© 2019. Published by The Company of Biologists Ltd | Journal of Cell Science (2019) 132, jcs232355. doi:10.1242/jcs.232355

RESEARCH ARTICLE

Concerted regulation of actin polymerization during constitutive secretion by cortactin and PKD2

Florian Weeber, Alexander Becher, Tanja Seibold, Thomas Seufferlein and Tim Eiseler*

ABSTRACT

Constitutive secretion from the trans-Golgi-network (TGN) is facilitated by a concerted regulation of vesicle biogenesis and fission processes. The protein kinase D family (PKD) has been previously described to enhance vesicle fission by modifying the lipid environment. PKD also phosphorylates the actin regulatory protein cortactin at S298 to impair synergistic actin polymerization. We here report additional functions for PKD2 (also known as PRKD2) and cortactin in the regulation of actin polymerization during the fission of transport carriers from the TGN. Phosphorylation of cortactin at S298 impairs the interaction between WIP (also known as WIPF1) and cortactin. WIP stabilizes the autoinhibited conformation of N-WASP (also known as WASL). This leads to an inhibition of synergistic Arp2/3-complex-dependent actin polymerization at the TGN. PKD2 activity at the TGN is controlled by active CDC42-GTP which directly activates N-WASP, inhibits PKD2 and shifts the balance to non-S298-phosphorylated cortactin, which can in turn sequester WIP from N-WASP. Consequently, synergistic actin polymerization at the TGN and constitutive secretion are enhanced.

KEY WORDS: PKD2, PRKD2, Cortactin, N-WASP, Actin polymerization, Constitutive secretion

INTRODUCTION

Secretion is driven by highly dynamic processes that govern cargo sorting, carrier biogenesis and fission of various transport carriers from the Golgi compartment (Egea et al., 2006; Pfeffer, 2010). The actin cytoskeleton and its rapid changes in local network density are critical factors determining Golgi structure and biogenesis of Golgi-derived transport carriers (Egea et al., 2006). To this end, actin filaments and regulatory proteins are localized to and interact with Golgi membranes (Kienzle et al., 2014; Stamnes, 2002; Valderrama et al., 1998, 2001, 2000). One important function of the actin cytoskeleton at the Golgi compartment is the maintenance of cisternae continuity (Egea et al., 2006; Valderrama et al., 1998). Moreover, actin recruitment and polymerization facilitated by the Rho-GTPase CDC42 (Dubois et al., 2005; Luna et al., 2002; Matas et al., 2004), nucleation-promoting factors (NPFs), such as N-WASP (also known as WASL) (Alekhina et al., 2017; Bhattacharya et al., 2016; Matas et al., 2004), and nucleators, like the Arp2/3 complex (Dubois and Chavrier, 2005; Matas et al., 2004) as well as actin-regulatory proteins, for example, cortactin (Cao et al., 2005; Kessels and Qualmann, 2005) determine transport carrier budding and fission. Carrier separation is further facilitated by pinching-off vesicles through oligomerization of dynamin-2, which was also shown to interact with cortactin and recruit the nucleation promoting factor N-WASP (Cao et al., 2005; Shin et al., 2008). Additionally, cortactin facilitates post-Golgi transport processes (Cao et al., 2005). However, the molecular coordination between vesicle biogenesis and actin assembly processes during post-trans-Golgi-network (TGN) transport remains to be investigated in more detail. Arp2/3-mediated actin nucleation has been linked to AP-1 transport carrier fission from the TGN (Anitei et al., 2010), where N-WASP and Arp2/3-dependent actin polymerization towards membranes promotes tubule formation (Anitei et al., 2010). In addition, BAR-domain-containing proteins, dynamin-2 and cortactin have been reported to bind to tubular carriers in order to help maintain tubule elongation and fission (Anitei et al., 2010). Nucleation by the Arp2/3 complex requires activation through class I NPFs, like N-WASP, which utilize their respective verprolin homology (WASP homology 2, WH2) domains (Helgeson and Nolen, 2013). In resting cells, N-WASP is kept in an autoinhibited inactive state. The only physiological inhibitor of WASP-mediated actin assembly is the WAS/WASL-interacting protein family member 1 (WIP, also known as WIPF1) (Ho et al., 2004; Moreau et al., 2000; Ramesh and Geha, 2009; Takano et al., 2008). WIP can stabilize and sequester N-WASP in its inactive, auto-inhibited configuration (Ho et al., 2004; Ramesh and Geha, 2009). A number of proteins, including CDC42 or Src homology 3 (SH3) domain-containing proteins, such as Nck, Grb2, cortactin, and Toca-1, activate WASP family NPFs (Helgeson and Nolen, 2013; Ho et al., 2004; Kowalski et al., 2005; Mizutani et al., 2002; Scaplehorn et al., 2002; Tomasevic et al., 2007). N-WASP has been shown to localize to the Golgi complex, but its role at the TGN is controversial (Anitei et al., 2010; Matas et al., 2004). Cortactin is present at the TGN (Anitei et al., 2010; Kessels and Qualmann, 2005), but it is only a weak class 2 NPF, since it cannot recruit actin monomers to the Arp2/3-complex. In the presence of N-WASP, branching nucleation by cortactin is substantially increased, demonstrating a striking synergy between the two NPFs (Helgeson and Nolen, 2013). Thus, an obligatory displacement model has been proposed, whereby cortactin specifically targets nascent branch junctions to displace N-WASP, which stalls completion of nucleation by the Arp2/3 complex until it is removed by cortactin, providing an additional means of control over network branching (Helgeson and Nolen, 2013).

In order to aid in membrane-carrier budding and fission at the Golgi complex, local actin polymerization needs to be tightly controlled and precisely timed. This may be achieved by several molecular mechanisms, which include the regulation of phosphatidylinositol 4,5-bisphosphate (PIP2) levels (Higgs and Pollard, 2001; Rohatgi et al., 2000; Tomasevic et al., 2007) and regulation of CDC42 activity by GTPase-activating proteins

Department of Internal Medicine I, Ulm University, Albert-Einstein-Allee 23, D-89081 Ulm, Germany.

*Author for correspondence (tim.eiseler@uniklinik-ulm.de)

F.W., 0000-0003-3837-5265; A.B., 0000-0003-1552-1581; T.Seufferlein, 0000-0003-3259-0810; T.E., 0000-0001-7819-4659

Received 26 March 2019; Accepted 7 November 2019

Journal of Cell Science (2019) 132, jcs232355. doi:10.1242/jcs.232355

(GAPs) or guanine nucleotide exchange factors (GEFs) (Dubois et al., 2005; Estrada et al., 2001; Ménétrey et al., 2007). Our group and others have previously described another important regulator of vesicle fission at the TGN: protein kinase D (PKD) (Baron and Malhotra, 2002; Cruz-Garcia et al., 2013; Eiseler et al., 2016; Ghanekar and Lowe, 2005; Hausser et al., 2005; Liljedahl et al., 2001; Malhotra and Campelo, 2011; Pusapati et al., 2010). PKD kinases phosphorylate substrates, such as phosphatidylinositol-4 kinase IIIβ (PI4K3β) (Hausser et al., 2005) and CERT (Fugmann et al., 2007) to alter the lipid environment in order to facilitate vesicle scission from the TGN. Moreover, we have reported a phosphorylation independent interaction of PKD2 (also known as PRKD2) with the vital GTPases ARF1 and ARL1, governing vesicle biogenesis processes at the TGN (Eiseler et al., 2016; Pusapati et al., 2010). Moreover, dimers between PKD2 and PKD3 (also known as PRKD3) isoforms have been reported to coordinate secretion from the TGN (Bossard et al., 2007). Interestingly, PKDs also control actin nucleation and polymerization via their substrate cortactin (Eiseler et al., 2010). Cortactin is phosphorylated by PKD at S298, impairing actin nucleation by the Arp2/3 complex *in vitro* (Eiseler et al., 2010). Here, we investigated whether PKD2 is also involved in tuning and timing actin polymerization processes during vesicle scission at the TGN via its substrate cortactin.

RESULTS

Key regulators of actin polymerization are localized at the TGN

In addition to a wide subcellular distribution near the plasma membrane, in the cytoplasm and at the Golgi complex, the Arp2/3 actin nucleation complex and cortactin have been reported to partially localize at the TGN, (Anitei et al., 2010). In accordance with these results, we also find perinuclear enrichment and partial colocalization of endogenous Arp2 and cortactin with the trans-Golgi markers TGN-46 and golgin-97 (also known as TGOLN2 and GOLGA1, respectively) (Eiseler et al., 2016), respectively (Fig. 1A,B). We also show a partial colocalization of cortactin–GFP with endogenous dynamin at golgin-97-positive compartments, which is in line with a putative implication of cortactin during vesicle fission (Anitei et al., 2010) (Fig. 1C). A role during carrier biogenesis at the TGN has also been described for the nucleation-promoting factor N-WASP (Anitei et al., 2010). N-WASP is an important activator of the Arp2/3 complex (Higgs and Pollard, 2001; Ti et al., 2011). However, a localization of N-WASP at the TGN is controversially debated, since ectopically expressed N-WASP–GFP was also shown to localize at the cis-Golgi compartment, and not the TGN (Matas et al., 2004). In order to investigate the TGN localization of endogenous N-WASP with higher resolution and contrast, we utilized Huygens classic maximum likelihood estimation (CMLE) deconvolution. Indeed, we were able to demonstrate signal enrichment at golgin-97-positive structures, enabling a putative role for N-WASP in modulating Arp2/3 complex-mediated actin dynamics at the TGN (Fig. 1D). Staining specificity was validated in N-WASP-depleted cells. (Fig. S1A). We also quantified colocalization of cortactin and N-WASP with golgin-97 in confocal image sections, respectively. Statistical analysis corroborated partial colocalization with TGN membranes, as indicated by a mean Pearson's colocalization coefficient (PCC) of 0.22 for cortactin and of 0.495 for N-WASP (Fig. 1E). The more-prominent colocalization of N-WASP with golgin-97 may be explained by direct membrane anchoring of N-WASP through interaction with PIP2 lipids (Papayannopoulos et al., 2005), whereas cortactin is not known to directly associate with Golgi membranes (Schnoor et al., 2018). To verify a broader function of the respective proteins at the TGN, we have further investigated colocalization of Arp2 with TGN46 as well as of cortactin and N-WASP with golgin-97 in differentiated polarized endothelial monolayers (Fig. S1B–D). These data indicated a partial colocalization with TGN membranes, suggesting a role for cortactin, N-WASP and the Arp complex during actin remodeling at the TGN.

PKD and cortactin interact at the TGN

During endocytosis, carrier biogenesis and scission from the plasma membrane is supported by the generation of branched actin networks that aid in carrier biogenesis and exert forces on vesicles to facilitate fission (Qualmann et al., 2000; Smythe and Ayscough, 2006). Similar actin networks are thought to drive carrier scission at the TGN, as demonstrated for AP-1 tubular carriers by Anitei et al. (2010). PKD regulates actin polymerization and formation of branched actin networks by the Arp2/3 complex via phosphorylation of the actin-regulatory protein cortactin at S298 (Eiseler et al., 2010). A connection of PKD2 to vesicle biogenesis and fission cycles at the TGN, established previously by our group and others (Eiseler et al., 2016; Hausser et al., 2005; Pusapati et al., 2010), prompted us to investigate whether phosphorylation of cortactin by PKD2 might be involved in controlling actin polymerization and constitutive secretion from the TGN. To this end, we first performed proximity ligation assays (PLA) to visualize the molecular proximity of endogenous PKD2 and cortactin at TGN structures, using confocal microscopy (Fig. 2A,B). During these experiments, furin–GFP was used to identify the TGN as indicated by quantitative colocalization with TGN46 and golgin-97 (PCC of 0.77), whereas the TGN markers showed a PCC of 0.79 (Fig. S2A). We further validated molecular proximity/interaction of PKD2–GFP and endogenous cortactin at golgin-97-positive structures using acceptor-photobleach Förster resonance energy transfer (AB-FRET). GFP and PKD2-P275G–GFP, which is no longer effectively recruited to the TGN (Pusapati et al., 2010), were used as respective negative controls for AB-FRET experiments (Fig. 2C,D). Additionally, we employed co-immunoprecipitation (co-IP) experiments to generally recapitulate an interaction of PKD2–GFP with endogenous cortactin (Fig. 2E,F). At the TGN, formation of PKD2–PKD3 dimers has been reported to coordinate secretion (Bossard et al., 2007). We have previously shown that PKD1 and PKD2 can phosphorylate cortactin (Eiseler et al., 2010). To test, whether endogenous PKD3 also phosphorylates cortactin, we performed additional experiments using *PRKD3*-depleted HeLa CRISPR cells. As shown in IP experiments in (Fig. S2B), depletion of PKD3 impaired phosphorylation of endogenous cortactin at S298. Thus, these data suggest that PKD2–PKD3 dimers could be also implicated in regulating cortactin functions by means of phosphorylation at S298.

Active CDC42 inhibits PKD2 activity at the TGN

The Rho-GTPase CDC42 also localizes to the TGN (Musch et al., 2001). CDC42 activates Arp2/3-complex-mediated actin polymerization through N-WASP (Bhattacharya et al., 2016; Prehoda et al., 2000; Rohatgi et al., 2000) and our data indicate that N-WASP is partially localized at the TGN. Phosphorylation of cortactin at S298 by PKD2 impairs synergistic actin polymerization *in vitro* (Eiseler et al., 2010). This prompted us to investigate, whether CDC42 could inhibit PKD activity and thereby the inhibitory phosphorylation of cortactin. Indeed, inhibition of CDC42 activity in HEK293T cells, using the specific CDC42 inhibitor ML141 (Hong et al., 2013), resulted in significantly

Journal of Cell Science (2019) 132, jcs232355. doi:10.1242/jcs.232355

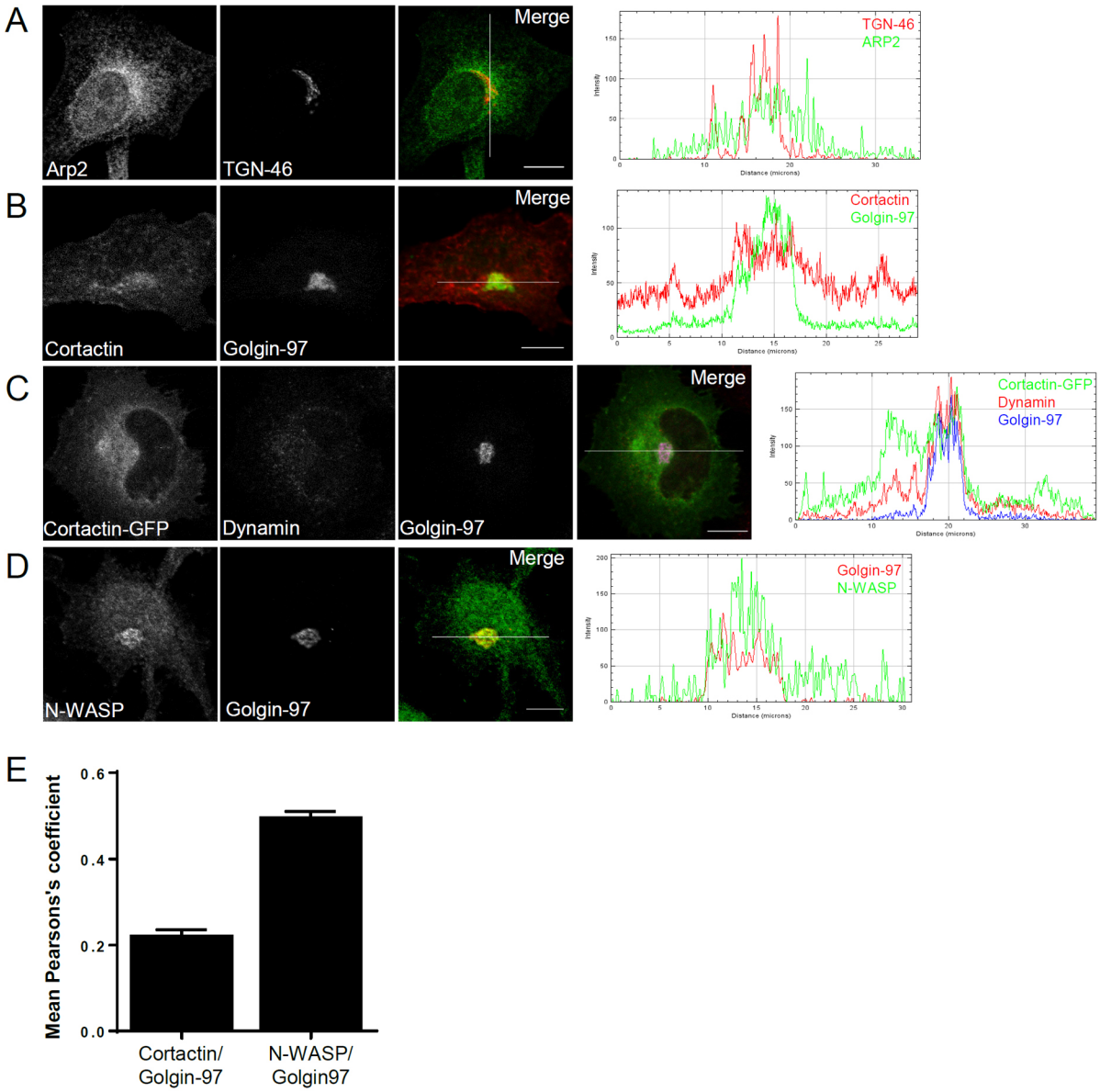

Fig. 1. Key regulators of actin polymerization are localized at the TGN. (A) Arp2 partially localizes to TGN46-positive structures. HeLa cells were stained for endogenous TGN-46 and Arp2. (B) Endogenous cortactin partially localizes to golgin-97-positive structures in HeLa cells. (C) Cortactin–GFP partially colocalizes with endogenous dynamin at golgin-97-positive structures in HeLa cells. (D) Endogenous N-WASP shows partial enrichment at golgin-97-positive structures in HeLa cells as revealed by deconvolution with the Huygens classic maximum likelihood estimation algorithm (CMLE). In A–D, all images depict confocal sections. Line intensity profiles shown on the right indicate colocalization. Scale bars: 10 µm. (E) Statistical analysis of quantitative colocalization for cortactin or N-WASP with golgin-97 in HeLa cells, respectively. The graph depicts the mean±s.e.m. PCC (*n*=42 cells, three experiments).

enhanced PKD activity, as demonstrated by increased its increase autophosphorylation at S916 (pS916) (Fig. 3A,B). Activation of PKD2 at the TGN in HeLa cells, which predominantly express PKD2 (Yeaman et al., 2004), was quantified upon treatment with ML141 by analyzing pS916 autophosphorylation using quantitative immunofluorescence. These experiments indicated significantly enhanced PKD activity upon inhibition of CDC42 at the TGN (2.29-fold), but also in the peripheral cytoplasm of cells (2.08-fold) (Fig. 3C,D). To further address an isoform-selective PKD2 activation at the TGN, we quantified PKD2 activation by measuring the FRET between PKD2–GFP and the anti-pPKD-S742/744 activation loop antibody, labeled with Alexa-Fluor-568 secondary antibodies, with and without co-expression of constitutively active CDC42-Q61L or inactive CDC42-T17N (Fig. S2C,D). In line with the ML141 experiments, inactive CDC42-T17N significantly enhanced PKD2 activity at the TGN, as demonstrated by increased percentage FRET values with respect to vector controls, whereas constitutively active CDC42-Q61L markedly inhibited PKD activity (Fig. S2D). These data demonstrate that the important actin-regulatory GTPase CDC42 can act upstream of PKD2 at the TGN.

CDC42, PKD2 and cortactin control actin polymerization at the TGN in an N-WASP-dependent manner

To determine whether CDC42, PKD2, cortactin and N-WASP are implicated in regulating actin polymerization at the TGN, we measured LifeAct–Ruby (Riedl et al., 2008) fluorescence intensities over time, as a marker for F-actin formed under steady-state

Journal of Cell Science (2019) 132, jcs232355. doi:10.1242/jcs.232355

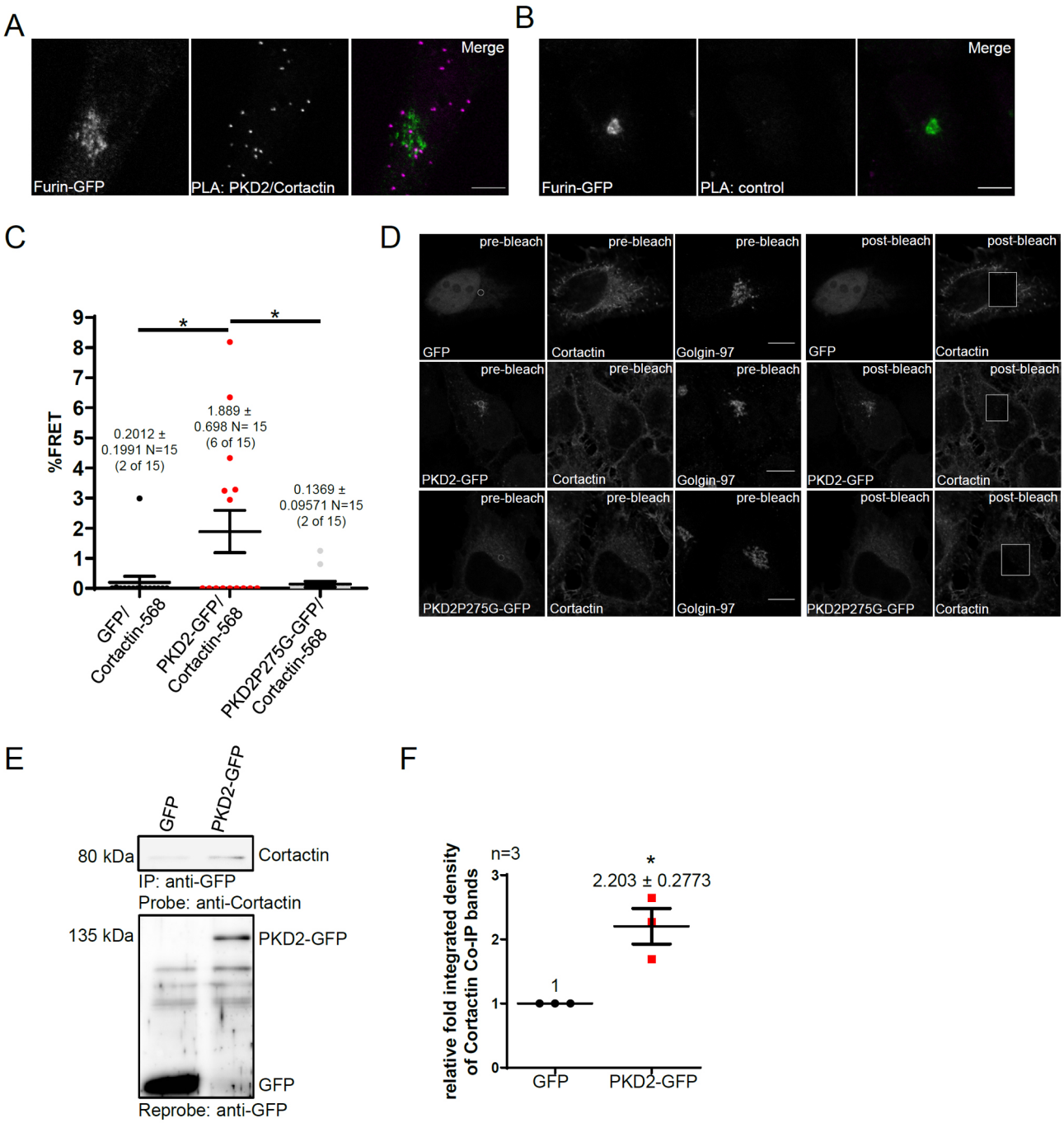

Fig. 2. PKD2 and cortactin interact at the TGN. (A) PLA with PKD2 and endogenous cortactin in HeLa cells. Molecular proximity was partially detected at furin–GFP-positive TGN structures. (B) Negative control for the PLA in A. The primary antibody against cortactin was omitted during these PLA experiments. In A and B, images depict single confocal sections. Scale bars: 10 µm. (C) Quantitative AB-FRET analysis for the interaction of PKD2–GFP and endogenous cortactin stained with anti-cortactin and Alexa-Fluor-568-conjugated antibodies at golgin-97-positive structures stained with Alexa-Fluor-647-conjugated secondary antibodies in HeLa cells. The graph shows mean±s.e.m. percentage FRET for *n*=15 cells from three independent experiments. A single detection region of interest (ROI) was placed on golgin-97-positive structures. GFP and PKD2-P275G–GFP were used as a negative controls. **P*<0.05 (one-way ANOVA with Tukey's post-test). (D) Representative images of AB-FRET experiments described in C. Left-hand side, pre-bleach images of donor (GFP, PKD2-GFP or PKD2-P275G–GFP), acceptor (cortactin), and golgin97 (TGN marker) as well as the ROI for quantification are shown. Right-hand side: post-bleach images of donor and acceptor with respective bleach ROIs. Scale bars: 10 µm. (E) Co-immunoprecipitation of PKD2 and cortactin in HEK293 T cells. Total cell lysates (TCLs) were subjected to immunoprecipitation (IP) with anti-GFP antibody and endogenous cortactin was detected in western blots using an anti-cortactin antibody. IPs were re-probed with anti-GFP antibody. (F) Quantification and statistical analysis of western blots from E. The graph shows mean±s.e.m. of three independent experiments. **P*<0.05 (two-tailed paired Student's *t*-test).

conditions. A baseline for detection of fluorescence intensities was set by bleaching the LifeAct signal at the TGN, indicated by furin–GFP. To validate LifeAct–Ruby measurements, we first evaluated F-actin intensity upon co-expression of the constitutively active CDC42-Q61L as well as upon knockout of PKD2 by CRISPR/Cas9 in HeLa cells. The PKD2-knockout (KO) was verified on the protein

Journal of Cell Science (2019) 132, jcs232355. doi:10.1242/jcs.232355

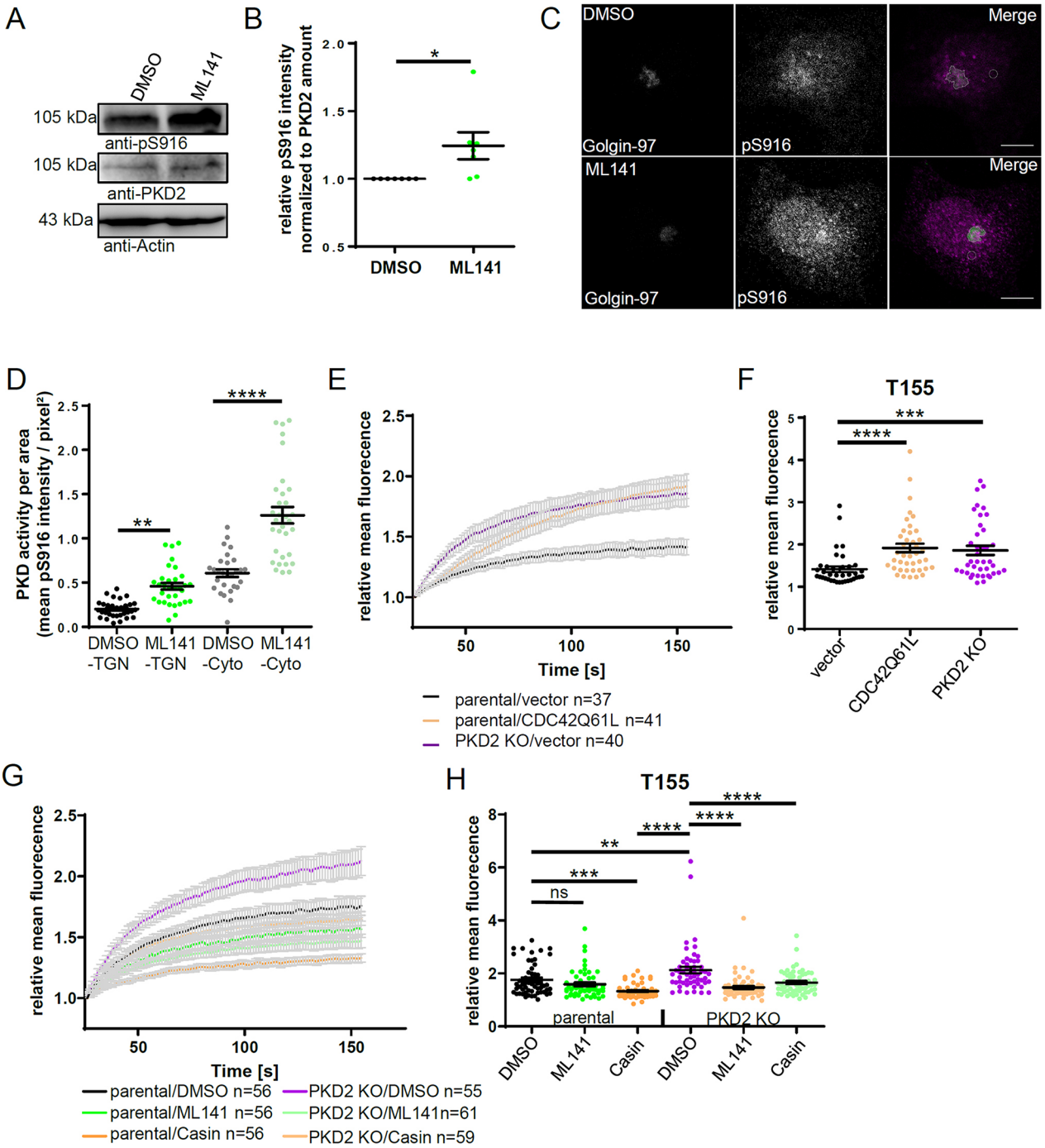

Fig. 3. CDC42 can inactivate PKD2 and facilitate actin polymerization at the TGN. (A) CDC42 inhibition increases PKD activity. HEK293T cells were treated for 1 h with 10 µM ML141 or DMSO. PKD activity was determined via western blotting using the anti-PKD pS916 autophosphorylation antibody (recognizing the active form). A PKD2-specific antibody was used to access total protein level. (B) Quantification and statistical analysis of western blots from A for n=7 experiments. *P<0.05 (two-tailed paired Student's t-test). (C) The CDC42 inhibitor ML141 increases PKD activity at the TGN. HeLa cells were treated with ML141 and stained for anti-PKD pS916 autophosphorylation as well as golgin-97. Images were acquired with equal settings using a confocal laser-scanning microscope. PKD activity was assessed by determining the mean fluorescence intensity of pS916 signals at golgin-97-positive structures. Golgin-97 was used to segment masks for quantification. TGN and cytoplasmic detection ROIs are shown. Images depict single confocal sections. Scale bars: 10 µm. (D) Statistical analysis of mean of ROI intensities from C. The graph depicts mean±s.e.m. of three independent experiments (n=31 cells for DMSO, n=32 for ML141). **P<0.01; ****P<0.0001 (one-way ANOVA with Tukey's post-test). (E) Actin polymerization at the TGN was measured by recording the F-actin signal over time by determining the LifeAct–Ruby signal at furin–GFP-positive structures after setting a baseline for detection by bleaching the LifeAct–Ruby signal. HeLa or HeLa PKD2 KO cells were transfected with the indicated plasmids as well as furin–GFP and LifeAct–Ruby. The final time point (t=155 s; T155) was used for statistical analysis. (F) Statistical analysis of FRAP experiments from E at T155. The graph depicts mean±s.e.m. of three independent experiments. ***P<0.001; ****P<0.0001 (Kruskal–Wallis test compared to parental/vector with Dunn's post-testing). (G) Inhibition of CDC42 activity by ML141 and casin impairs the LifeAct–Ruby signal recovery at the TGN under steady-state conditions in HeLa parental and PKD2 KO cells. (H) Statistical analysis of FRAP experiments from G at T155. The graph depicts mean±s.e.m. from at least four independent experiments. **P<0.01; ***P<0.001; ****P<0.0001; ns, not significant (one-way ANOVA with Tukey's post-test).

Journal of Cell Science (2019) 132, jcs232355. doi:10.1242/jcs.232355

level (Fig. S2E) and impaired secretion was demonstrated by evaluating secretion of the artificial cargo HRP (Fig. S2F). In line with the vital functions of PKD2 in modulating the lipid environment during vesicle fission at the TGN, HRP secretion from PKD2 KO cells was significantly impaired with respect to parental controls. Moreover, both active CDC42 and PKD2 knockout significantly increased mean LifeAct–Ruby fluorescence at the end of the 130 s recovery period (t=155 s), indicating enhanced steady-state F-actin generation (Fig. 3E,F; Fig. S3A,B, Movies 1–3).

Next, we determined steady-state F-actin at the TGN upon inhibition of CDC42 in parental and PKD2 KO cells using two specific CDC42 inhibitors: ML141 (10 µM) (Hong et al., 2013; Surviladze et al., 2010) and casin (5 µM) (Florian et al., 2012). We verified the inhibition of CDC42 by active CDC42-PBD-pulldown assay (Fig. S3C). Indeed, inhibition of CDC42 activity by both inhibitors significantly impaired actin polymerization at the TGN in PKD2KO cells, where F-actin turnover was reduced back to basal cell levels (Fig. 3G,H; Fig. S3D). In parental cells, Casin significantly reduced F-actin formation, whereas ML141 treatment showed a non-significant reduction of actin polymerization at the TGN. Thus, our data indicate that CDC42 can act upstream of PKD2 to control actin dynamics at the TGN.

We also investigated, whether ectopic expression of PKD2 inhibits actin polymerization in parental and PKD2 KO cells. Overexpression of PKD2 strongly decreased LifeAct–Ruby signals at the TGN in parental cells. In PKD2 KO cells, F-actin signals were significantly increased and re-expression of PKD2 was able to partially reverse this phenotype (Fig. 4A,B; Fig. S3E,F, Movies 4–7).

We then tested, whether enhanced generation of F-actin at the TGN in PKD2 KO cells was significantly reversed to parental with si*LacZ* (parental/si*LacZ*) levels by depletion of cortactin (si*CTTN*) (Fig. 4C,D; Fig. S3G,H, Movies 8–11). Indeed, cortactin knockdown in PKD2 KO cells significantly impaired steady-state actin polymerization to basal levels. In parental cells, depletion of cortactin also reduced formation of F-actin; however, changes were not statistically significant. Thus, these data demonstrate that cortactin is indeed implicated in enhanced actin polymerization at the TGN, controlled by PKD2.

We have previously demonstrated *in vitro* that cortactin that is not phosphorylated at S298A enhances synergistic actin polymerization by the Arp2/3-complex in the presence of an NPF (Eiseler et al., 2010), such as N-WASP. Phosphorylation of cortactin at S298 was further shown to generate a 14-3-3β-binding site (Eiseler et al., 2010). As the binding and biological effects of 14-3-3 proteins are strictly dependent on the presence of a phosphorylated residue (Mackintosh, 2004; Muslin and Xing, 2000; Sroka et al., 2016; Wille et al., 2018), we were unable to use serine to glutamate phosphorylation-mimicking mutations in all further experiments.

To evaluate a role for N-WASP in synergistic nucleation at the TGN, cortactin and cortactin-S298A were ectopically expressed in control and *WASL* (N-WASP) knockdown cells. Expression of cortactin-S298A significantly enhanced LifeAct fluorescence compared to cells with vector alone and or expressing wild-type cortactin. Strikingly, knockdown of *WASL* significantly reversed F-actin generation in cortactin-S298A-expressing cells compared to vector controls (Fig. 4E,F; Fig. S4A,B), pointing to a regulation by N-WASP and PKD2-phosphorylated cortactin.

The formation of actin at the Golgi complex, and in particular at the TGN, is not easily visualized or quantified (Gurel et al., 2014). As a second, independent method to evaluate relative steady-state actin polymerization (i.e. that was not dependent on the expression of LifeAct), we measured actin–GFP incorporation into phalloidin–Alexa-Fluor-568-labeled filaments at TGN-46-positive structures with AB-FRET (Sroka et al., 2016). We opted to utilize this previously published FRET approach (Sroka et al., 2016) to acquire specificity for nascently generated F-actin signals, since neither actin–GFP nor phalloidin–Alexa-568 alone displayed strong enrichment at the TGN (Fig. S4C,D). Indeed, in line with our LifeAct-FRAP experiments, we found that expression of constitutively active CDC42-Q61L significantly enhanced actin incorporation into filaments, whereas inactive CDC42-T17N impaired actin polymerization below vector levels. The latter changes were however not substantial enough to generate significant differences from the control condition. Of note, knockdown of *WASL* upon co-expression of CDC42-Q61L impaired actin polymerization to levels that were no longer significantly different from those in the vector controls (Fig. S4C), confirming validity of the FRET approach (Sroka et al., 2016) as a second method to determine relative actin turnover at the TGN. In additional experiments, only cortactin-S298A, but not wild-type cortactin significantly enhanced percentage FRET values and thus steady-state actin polymerization, whereas knockdown of *WASL* in cortactin-S298A-expressing cells reduced actin–GFP incorporation to vector control levels (Fig. S5A,B).

In summary, our analysis of actin polymerization at the TGN suggest that active PKD2 inhibits F-actin formation by phosphorylation of cortactin. We also show, that activation of CDC42 inactivates PKD2 and triggers signaling events that facilitate Arp2/3-complex-mediated synergistic actin polymerization in the presence of non-S298-phosphorylated cortactin in conjunction with the resident NPF N-WASP.

PKD2, cortactin and N-WASP regulate constitutive secretion from the TGN

Since we were able to show cortactin-S298-phosphorylation-dependent changes in actin turnover/polymerization at the TGN, we were prompted to investigate whether this would also translate into differences in constitutive secretion. To this end, we performed secretion experiments using the artificial substrate secreted horseradish peroxidase (HRP) (Cruz-Garcia et al., 2013; Fugmann et al., 2007) upon knockdown of *PRKD2* (PKD2) and *CTTN* (cortactin) using two different shRNAs in HEK293T cells (Fig. 5A; Fig. S6A). In line with our previous data (Eiseler et al., 2016; Pusapati et al., 2010), depletion of *PRKD2* (sh*PRKD2*) impaired constitutive secretion of HRP. Moreover, knockdown of *CTTN* (sh*CTTN*) also significantly impaired constitutive secretion (Fig. 5A; Fig. S6A). Similar to what was found for steady-state F-actin generation at the TGN, only the non-phosphorylatable cortactin-S298A enhanced constitutive secretion of HRP (Fig. 5B; Fig. S6B). To corroborate these data, we further measured constitutive secretion of the endogenous cargo MMP2 (Eiseler et al., 2016) from NIH 3T3 fibroblasts (Fig. 5C,D). Again, only non-S298-phosphorylatable cortactin significantly increased constitutive MMP2 secretion and concomitantly decreased cellular MMP2 levels (Fig. 5D).

Next, we evaluated the role of N-WASP during constitutive secretion by measuring HRP release. Ectopic expression of cortactin-S298A significantly increased constitutive secretion compared to wild-type cortactin, whereas secretion was significantly impaired upon depletion of endogenous *WASL*. Indeed, knockdown of *WASL* impaired constitutive secretion by the cortactin-S298A mutant to levels that were no longer significantly different from wild-type cortactin (Fig. 5E; Fig. S6C). This suggests that cortactin and N-WASP are likely to cooperate not only during regulation of

Journal of Cell Science (2019) 132, jcs232355. doi:10.1242/jcs.232355

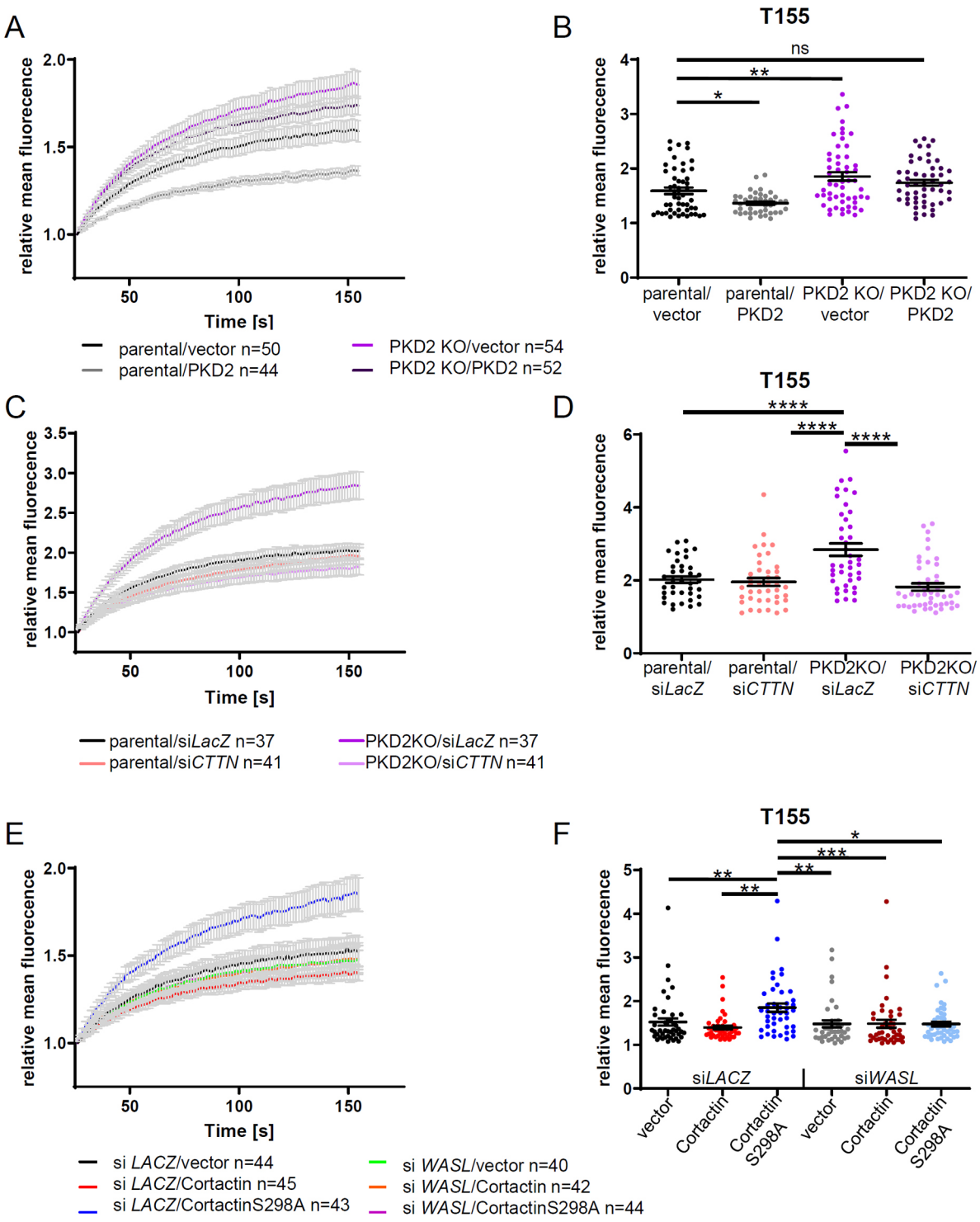

Fig. 4. PKD2 and cortactin regulate actin polymerization at the TGN in an N-WASP-dependent manner. (A) PKD2 KO increases F-actin at the TGN under steady-state conditions. HeLa parental or HeLa PKD2 KO cells were transfected with plasmids encoding furin–GFP, LifeAct–Ruby, vector or PKD2. (B) Statistical analysis of FRAP experiments from A at *t*=155 s (T155). The graph depicts mean±s.e.m. of four independent experiments. Outliers were removed using the method of ROUT (Q=5%). **P*<0.05; ***P*<0.01; ns, not significant (one-way ANOVA with Dunnett's post-test compared to the parental/vector condition). (C) Depletion of cortactin reverses the F-actin increase at the TGN under steady-state conditions in PKD2 KO cells. HeLa parental or HeLa PKD2 KO cells were transfected 48 h prior to experiments with si*LACZ* and si*CTTN* as well as plasmids encoding furin–GFP and LifeAct–Ruby. (D) Statistical analysis of FRAP experiments from C at T155. The graph depicts mean±s.e.m. of at least three independent experiments. *****P*<0.0001 (one-way ANOVA with Tukey's post-test). (E) Depletion of N-WASP reverses the F-actin increase at the TGN under steady-state conditions in cortactin-S298A-expressing cells. HeLa cells were transfected 48 h prior to experiments with si*LACZ* or si*WASL* and furin–GFP, LifeAct–Ruby as well as the indicated constructs. (F) Statistical analysis of FRAP experiments from E at T155. The graph depicts mean±s.e.m. of three independent experiments. **P*<0.05; ***P*<0.01; ****P*<0.001 (one-way ANOVA with Tukey's post-test).

Journal of Cell Science (2019) 132, jcs232355. doi:10.1242/jcs.232355

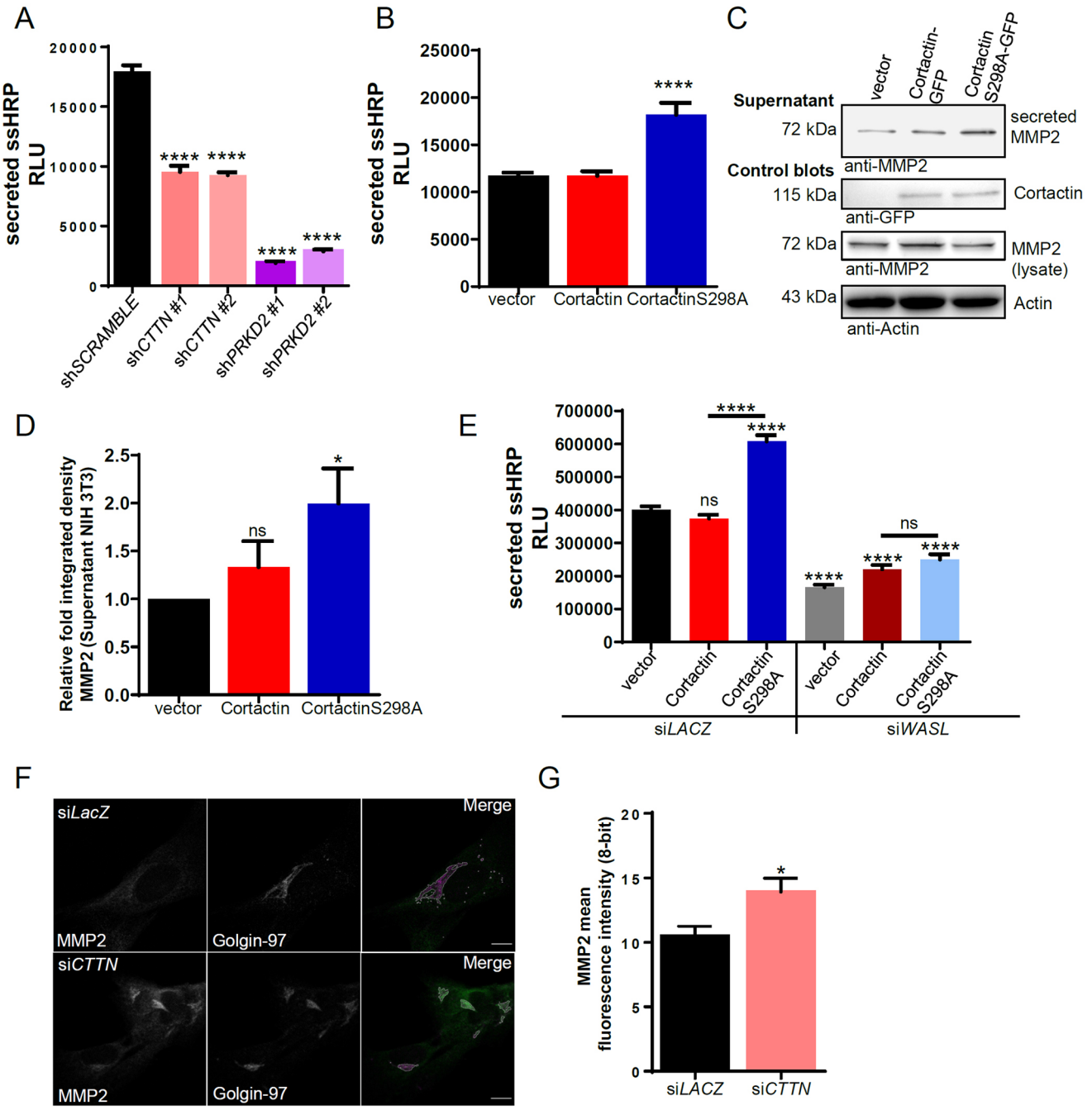

Fig. 5. PKD2, cortactin and N-WASP regulate constitutive secretion. (A) Knockdown of *PRKD2* and *CTTN* reduces secretion of signal sequence (ss)HRP from semi-stable HEK293T knockdown lines transfected with an HRP expression vector. Following 16 h of expression, HRP was collected in the culture supernatant for 4 h and incubated with ECL solution (results are given as relative light units, RLU). The graph shows mean±s.e.m. of six independent experiments with three technical replicas (n=18). ****P<0.0001 (one-way ANOVA with Dunnett's post-tests compared with sh*SCRAMBLE*). (B) Expression of cortactin-S298A increases HRP secretion. HEK293T cells were co-transfected with GFP–vector, cortactin–GFP or cortactin-S298A–GFP and HRP at a ratio of 3:1. The graph shows mean±s.e.m. of six independent experiments with three technical replicas (n=18). ****P<0.0001 (one-way ANOVA with Dunnett's post-tests compared with vector). (C) Expression of cortactin-S298A increases secretions of endogenous MMP2 from NIH 3T3 fibroblasts, transfected with GFP, cortactin–GFP and cortactin-S298A–GFP. After 24 h, MMP2 was accumulated in 900 µl of serum-free medium for 24 h. Supernatants and cells analyzed by western blotting for the presence of MMP2 or ectopic cortactin, respectively. (D) Statistical analysis of western blots from C. The graph shows mean±s.e.m. of nine independent experiments. *P<0.05; ns, not significant (one-way ANOVA with Tukey's post-test). (E) The cortactin-S298A-mediated increase in secretion is N-WASP-dependent. HEK293T cells were transfected with si*LACZ* or si*WASL* together with HRP. The next day, cells were transfected with GFP-vector, cortactin-GFP or cortactin-S298A–GFP constructs. At 48 h after the first transfection, HRP secretion was analyzed. The graph shows mean±s.e.m. of five independent experiments with three technical replicas (n=15). ****P<0.0001; ns, not significant (one-way ANOVA with Dunnett's post-test compared with si*LACZ*/vector). (F) Retention of endogenous MMP2 at the TGN upon depletion of cortactin. WI-38 fibroblasts were transfected with si*LACZ* and si*CTTN*. After 48 h, images were acquired with equal settings using a confocal laser-scanning microscope. Intensity of endogenous MMP2 at the TGN was assessed by measuring signals at golgin-97-positive structures. Golgin-97 was used to segment masks for quantification by mean of ROI analysis. TGN ROIs are shown in images. Images depict single confocal sections. Scale bars: 10 µm. (G) Statistical analysis of quantitative microscopy from F. The graph shows mean±s.e.m. of three independent experiments, n=105 cells for si*LACZ* and n=112 cells for si*CTTN*. *P<0.05 (two-tailed unpaired Student's t-test).

synergistic actin polymerization at the TGN (Fig. 4D,F) but also in the regulation of PKD2-controlled constitutive secretion (Fig. 5E). Moreover, these data are supported by evaluating secretion of endogenous MMP2 from NIH 3T3 fibroblasts. Here, knockdown of the mechano-GTPase dynamin-2 (*DNM2*), N-WASP (*WASL*) and cortactin (*CTTN*) significantly impaired secretion by 63.1%, 55.5% and 46.8%, respectively (Fig. S6D,E).

Finally, if vesicle release from TGN membranes were regulated by PKD2 and cortactin, depletion of cortactin would be expected to also result in cargo retention. To evaluate such an effect upon knockdown of *CTTN*, we quantified the fluorescence intensity of endogenous MMP2 at golgin97-positive structure in WI38 fibroblasts, which express high levels of MMP2 (Fig. 5F,G; Fig. S6F). In line with the HRP and MMP2 constitutive secretion data, we demonstrate increased MMP2 fluorescence at the TGN upon depletion of cortactin, suggesting that cortactin is required for proper cargo release (Fig. 5F,G).

Molecular control of actin polymerization by PKD2, cortactin and N-WASP

Our data demonstrated a functional role for synergistic actin polymerization initiated by cortactin and N-WASP at the TGN. *In vitro* pyrene-actin polymerization in the presence of the Arp2/3-complex, a GST-tagged VCA domain (minimal fragment of WASP) and purified cortactin or cortactin-S298A, indicated cortactin and its phosphorylation by PKD regulate synergistic actin polymerization with class I NPFs (Eiseler et al., 2010). However, cortactin is also implicated in the activation of full-length N-WASP, by relieving N-WASP autoinhibition (Kowalski et al., 2005). Thus, we next examined how phosphorylation of cortactin at S298 might regulate Arp2/3 complex activity at different levels. To this end we employed a CFP–N-WASP–YFP FRET biosensor (Lorenz et al., 2004b; Oser et al., 2009). This sensor indicates the extent of activated N-WASP by a concomitant loss of FRET during unfolding (Lorenz et al., 2004b). The biosensor was co-expressed with wild-type cortactin, cortactin-S298A or a vector control in HEK293T (Fig. 6A; Fig. S7A) and HeLa cells (Fig. S7B,C). Active N-WASP was determined by FRET in total cell lysates. We detected significantly increased levels of N-WASP in an active, open conformation upon co-expression of cortactin-S298A, in respect to wild-type cortactin. This suggests that PKD phosphorylation might be implicated in controlling N-WASP activation. We also evaluated N-WASP activity regulated by cortactin and cortactin-S298A in the perinuclear region of intact MCF-7 cells. The N-WASP-FRET biosensor was co-expressed with the respective constructs in MCF-7 cells, which are highly responsive to heregulin, and cells were stimulated to induce actin polymerization and secretion (Döppler et al., 2013; Eiseler et al., 2010). Again, N-WASP activity was significantly enhanced and more sustained upon co-expression of non-phosphorylatable cortactin-S298A (Fig. 6B). These data indicate that cortactin and its phosphorylation by PKD are not only implicated in modulating synergistic actin polymerization (Eiseler et al., 2010), but also in controlling the class I NPF activity of N-WASP.

Cortactin phosphorylation at S298 activates the N-WASP–WIP complex at the TGN

Given our above findings, we were interested to investigate how the activation of N-WASP is controlled at a molecular level. *In vivo*, N-WASP is sequestered in its inactive, autoinhibited state by the inhibitory binding protein WIP. *In vitro*, TOCA-1 (transducer of CDC42-dependent actin-assembly protein-1 homolog, also known as FNBP1L) is a potent, CDC42-dependent activator of the N-WASP–WIP complex, requiring a functional SH3 domain (Ho et al., 2004; Moreau et al., 2000). In addition, SH3 domains from a number of other proteins, such as Grb2 and Nck1/Nck2 are known to promote N-WASP activation (Campellone et al., 2012; Ho et al., 2004; Moreau et al., 2000). Similar functions have been described for the SH3 domain of cortactin (Kowalski et al., 2005). Thus, we examined further whether phosphorylation of cortactin at S298 by PKD2 might alter the molecular complex between N-WASP and WIP at the TGN.

Initially, we performed colocalization studies with mCherry–WIP and endogenous N-WASP in HeLa cells. Although, we did not detect an enrichment of WIP at golgin-97-positive structures, a partial colocalization was demonstrated utilizing Huygens confocal deconvolution microscopy (CLME) (Fig. 6C). To investigate localization and molecular proximity of endogenous proteins, we additionally performed PLAs for N-WASP and Arp2 (Fig. 6D,E), as well as N-WASP and WIP (Fig. 6F,G). PLA staining indicated a wide distribution of Arp2–N-WASP and N-WASP–WIP signals throughout the cell, which also included furin–GFP-positive structures (Fig. 6D–G). Thus, WIP is indeed present at the TGN. We therefore performed co-IP experiments with ectopically expressed proteins to assess changes in N-WASP–WIP interaction upon co-expression of vector, cortactin and cortactin-S298A. Ectopically expressed N-WASP was detected in endogenous WIP immunoprecipitations (IPs) when wild-type cortactin was co-expressed, but this interaction was lost upon co-expression of cortactin-S298A (Fig. 6H). Since it was previously reported that cortactin can also bind to WIP (Kinley et al., 2003), and enhanced its ability to act as an NPF, we were prompted to conduct co-IPs of cortactin or cortactin-S298A–FLAG with mCherry–WIP (Fig. 7A,B). Concomitant with a loss of N-WASP–WIP interaction, the binding of WIP to non-phosphorylated cortactin-S298A was significantly increased (Fig. 7A,B). We further verified that binding of WIP to cortactin was dependent on its SH3 domain (Kinley et al., 2003) (Fig. S7D). Molecular proximity of cortactin and WIP at the TGN was corroborated by PLA staining at furin–GFP-positive structures (Fig. 7C,D). To determine regulation of N-WASP activity by WIP and PKD2-cortactin at an endogenous level, we again performed co-IP experiments in parental and PKD2 KO HeLa cells. In line with experiments described above, PKD2 knockout resulted in a significantly impaired interaction of endogenous N-WASP and WIP, suggesting that this pathway is indeed utilized in cells (Fig. 7E,F). Thus, our data point to a mechanism whereby active PKD2 phosphorylates cortactin at S298 to block the activation of the N-WASP–WIP complex at the TGN (Figs 6D–H and 7A–F) until the lipid environment is ready for carrier fission. In order to acquire further quantitative evidence for such a regulation at the TGN, we performed AB-FRET interaction studies with N-WASP–GFP and endogenous WIP at TGN46-postive structures in HeLa cells. Cortactin–FLAG, cortactin-S298A–FLAG or empty vector were co-expressed to alter the N-WASP–WIP complex composition (Fig. 7G; Fig. S7E). In HeLa cells, N-WASP–GFP is localized in the cytoplasm, the perinuclear region and the nucleus (Mizutani et al., 2004; Suetsugu and Takenawa, 2003; Wu et al., 2004), which is comparable to what is seen for the endogenous protein, but TGN enrichment is less prominent, likely due to ectopic expression. We were therefore prompted to exclude strongly expressing cells from AB-FRET experiments in Fig. 7G and Fig. S7E. In line with the co-IPs and PLA experiments, AB-FRET analysis gave a significantly decreased percentage FRET value upon expression of cortactin-S298A for the interaction of N-WASP with endogenous WIP at the

Journal of Cell Science (2019) 132, jcs232355. doi:10.1242/jcs.232355

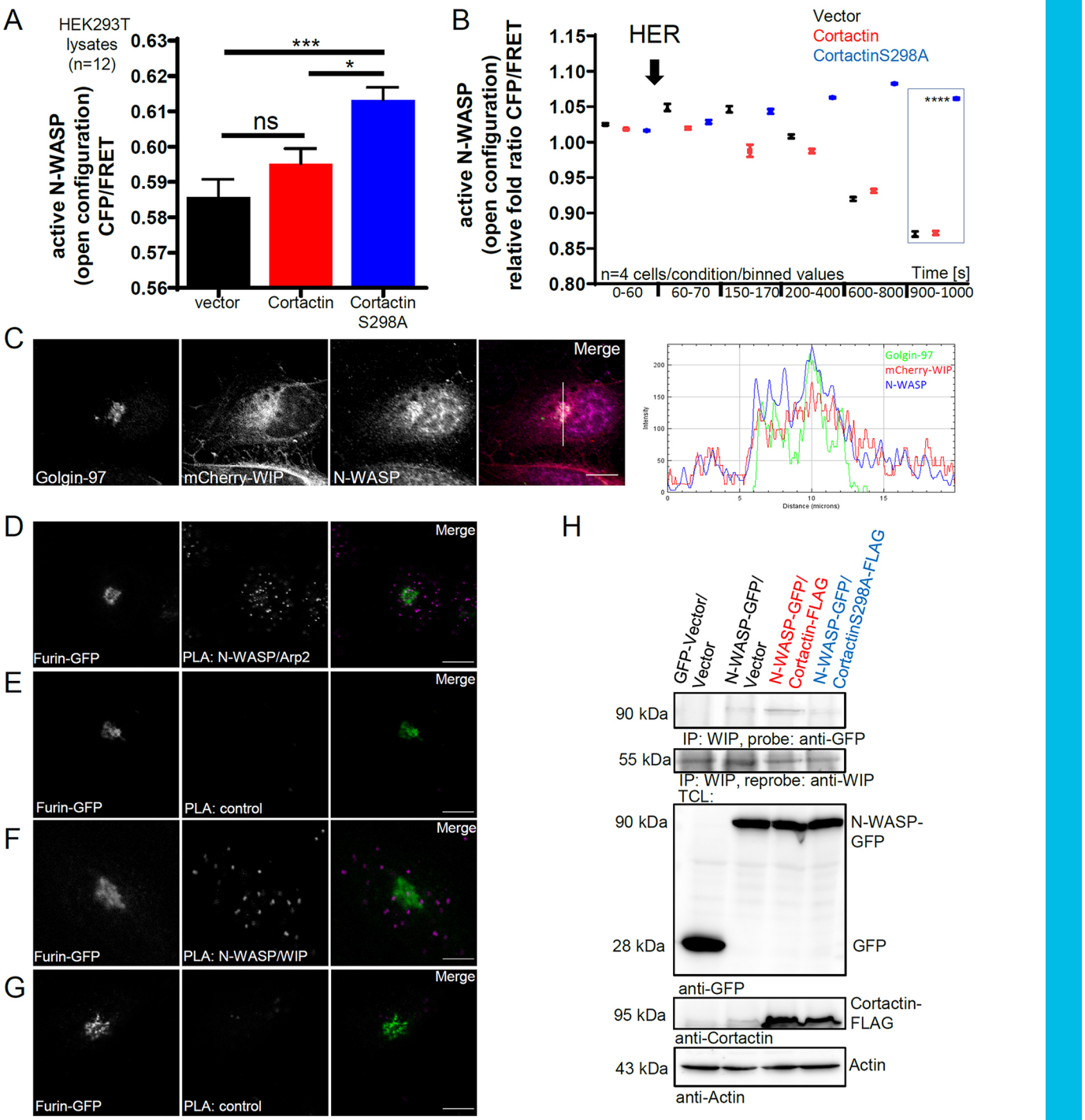

Fig. 6. Cortactin-S298A can activate N-WASP by sequestering WIP. (A) A CFP–N-WASP–YFP FRET activity sensor was co-transfected with the indicated constructs (1:3) in HEK293T cells. After 24 h, cells were lysed and fluorescence was measured in cleared lysates using a plate reader. The graph displays relative CFP:FRET ratios for *n*=12 independently transfected samples. (B) The N-WASP biosensor was co-transfected with the indicated constructs in MCF-7 cells. After 24 h, cells were serum-starved for 4 h and then subjected to live imaging using a LSM710 confocal microscope at 37°C and 5% CO_2. After 60 s, cells were stimulated with 100 ng/ml heregulin (HER). For statistical analysis, the mean of ROI intensities from *n*=4 independent experiments were binned as indicated on the *x*-axis. The graph displays relative CFP:FRET ratios. In A and B, **P*<0.05; *****P*<0.0001; ns, not significant (one-way ANOVA with Tukey's post-test). (C) N-WASP and WIP partially colocalize at the TGN. HeLa cells expressing mCherry–WIP were stained for endogenous golgin-97 and N-WASP. Images show single confocal sections after CMLE deconvolution. The right hand panel shows a line intensity profile indicating colocalisation. Scale bar: 10 µm. (D) PLA with endogenous N-WASP and Arp2 in HeLa cells. Molecular proximity was partially detected at furin–GFP-positive TGN structures. (E) Negative control for the PLA in D. The primary antibody against Arp2 was omitted during PLA experiments. (F) PLA with endogenous N-WASP and WIP in HeLa cells. Molecular proximity was partially detected at furin–GFP-positive TGN structures. (G) Negative control for the PLA in F. The primary antibody against WIP was omitted during PLA experiments. D–G images depict single confocal sections. Scale bars: 10 µm (D–G). (H) Cortactin-S298A disrupts binding between N-WASP and WIP. HEK293T cells expressing N-WASP–GFP and cortactin–FLAG, cortactin-S298A–FLAG or vector were subjected to co-IP experiments with an anti-WIP antibody. Subsequently, co-precipitated N-WASP–GFP was detected using an anti-GFP antibody. IPs were re-probed with anti-WIP. The lower panel shows total cell lysates (TCLs) probed for the presence of N-WASP–GFP and FLAG–cortactin. One of three independent experiments is shown.

Journal of Cell Science (2019) 132, jcs232355. doi:10.1242/jcs.232355

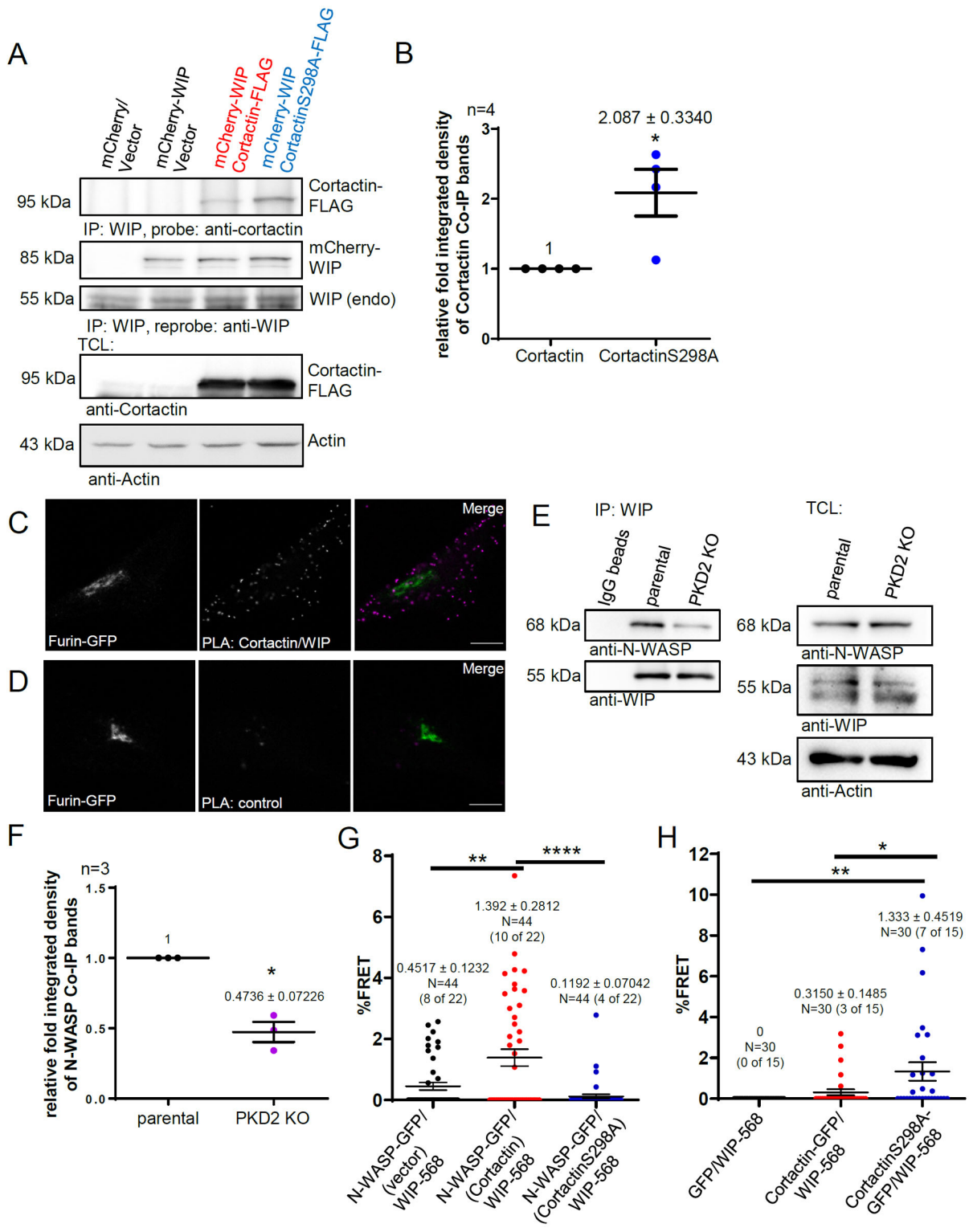

Fig. 7. See next page for legend.

TGN with respect to that found upon expression of wild-type cortactin (Fig. S7D,E). Moreover, we were able to detect an enhanced interaction of cortactin-S298A–GFP with endogenous WIP labeled with Alexa-Fluor-568-conjugated secondary antibodies at TGN46-postive structures (Fig. 7H; Fig. S7F). Thus, our AB-FRET experiments further verify and quantify the PKD-phosphorylation-dependent interaction of cortactin and WIP at the TGN and indicate a coordinated N-WASP activation through WIP sequestration.

DISCUSSION

Actin polymerization has been suggested to support biogenesis and scission of transport carriers from various locations, for example, during endocytosis (Anitei et al., 2010; Kessels and Qualmann,

Fig. 7. Cortactin-S298A sequesters WIP from N-WASP. (A) Binding of WIP to cortactin is enhanced for the non-phosphorylatable cortactin-S298A mutant. HEK293T cells expressing mCherry–WIP and cortactin–FLAG, cortactin-S298A–FLAG or vector were used for co-IPs with an anti-WIP antibody. Ectopically expressed cortactin was detected by an anti-cortactin antibody. IPs were re-probed with anti-WIP antibody. The lower panel shows total cell lysates (TCLs) probed for the expression of cortactin–FLAG and cortactin-S298A–FLAG. One of four independent experiments is depicted. (B) Quantification and statistical analysis of co-IP experiments from A. The graph shows mean±s.e.m. of four independent experiments. **P*<0.05 (two-tailed paired Student's *t*-test). (C) PLA with endogenous cortactin and WIP in HeLa cells. Molecular proximity was partially detected at furin–GFP-positive TGN structures. (D) Negative control for the PLA in C. The primary antibody against WIP was omitted during PLA experiments. In C and D images depict single confocal sections. Scale bars: 10 µm. (E) Binding of endogenous WIP and N-WASP is enhanced in PKD2 KO HeLa cells in respect parental controls. TCLs were subjected to co-IPs by precipitating WIP, and N-WASP was detected. IPs were re-probed with anti-WIP antibody. TCLs were probed for the expression of endogenous N-WASP and WIP. One of three independent experiments is depicted. (F) Quantification and statistical analysis of co-IP experiments from E. Co-IP bands were normalized to re-probed WIP. The graph shows mean±s.e.m. of three independent experiments. **P*<0.05 (two-tailed paired Student's *t*-test). (G) N-WASP and WIP interact at the TGN in a cortactin-S298-phosphorylation-dependent manner. Quantitative AB-FRET analysis in HeLa cells expressing N-WASP–GFP and vector, cortactin–FLAG or cortactin-S298A-FLAG, respectively. Cells were stained for endogenous WIP with anti-WIP and Alexa-Fluor-568-conjugated antibodies, whereas the TGN was labeled with anti-TGN46 and Alexa-Fluor-647-conjugated antibodies. The graph shows mean±s.e.m. percentage FRET for 22 cells and two equally sized detection ROIs at TGN46-positive structures from three independent experiments (*n*=44 ROIs). (H) Cortactin and WIP interact at the TGN in a cortactin-S298-phosphorylation-dependent manner. Quantitative AB-FRET analysis in HeLa cells expressing GFP, cortactin–GFP or cortactin-S298A–GFP. Cells were stained for endogenous WIP with anti-WIP and Alexa-Fluor-568-conjugated antibodies, whereas the TGN was labeled with anti-TGN46 and Alexa-Fluor-647-conjugated antibodies. The graph shows mean ±s.e.m. percentage FRET of 15 cells and two equally sized detection ROIs placed at TGN46-positive structures from three independent experiments (*n*=30 ROIs). **P*<0.05; ***P*<0.01; *****P*<0.0001 (one-way ANOVA with Tukey's post-test).

2005; Qualmann et al., 2000). At the TGN, the molecular composition and upstream regulation of branching actin polymerization still needs to be elucidated in more detail. In our present work, we show that the actin regulatory protein cortactin and its phosphorylation by PKD2 at S298 (Eiseler et al., 2010) are vital regulators of Arp2/3-complex-initiated actin polymerization at the TGN (Figs 2 and 4; Figs S4C,D and S5). In addition, N-WASP and its sequestering protein WIP (Ho et al., 2004) were shown to be localized at TGN structures by using a combination of colocalization studies, PLA experiments and FRET (Figs 1D,E, 6C–G and 7G; Fig. S7E). We show that phosphorylation of cortactin at S298 impairs the interaction of WIP and cortactin (Fig. 7A,B,H; Fig. S7F). WIP is known to stabilize the inactive autoinhibited conformation of N-WASP, preventing unsolicited nucleation by the Arp2/3-complex (Ho et al., 2004). Actin polymerization and N-WASP activity at the TGN are controlled downstream of the small GTPase CDC42 (Musch et al., 2001) (Fig. 3E–H; Fig. S3A-D). Active CDC42-GTP can directly activate N-WASP (Ho et al., 2004; Tomasevic et al., 2007) and disable a second level of inhibition by inactivating PKD2, thereby shifting the balance to non-S298-phosphorylated cortactin. Consequently, N-WASP sequestration in the autoinhibited state by WIP is disrupted (Figs 6H, 7E–H; Fig. S7E,F) and WIP binding to cortactin is enhanced (Fig. 7A,B,H; Fig. S7F), thus facilitating synergistic actin nucleation. We propose that the directional force generated by this precisely timed polymerization supports separation of transport carriers from the donor membrane, as we were able to demonstrate enhanced constitutive secretion upon expression of the non-S298-phosphorylated cortactin (Fig. 5B–D). Secretion was N-WASP dependent (Fig. 5E; Fig. S6D,E), and we show TGN retention of endogenous MMP2 cargo upon cortactin depletion (Fig. 5F,G).

Thus, phosphorylation of cortactin by PKD2 might regulate the timing of carrier fission steps (Fig. 8). Here, our data are in line with previously published work demonstrating a role for active PKD in modifying the TGN lipid environment to a fission-competent state (Fugmann et al., 2007; Hausser et al., 2005). As long as PKD is active, there is inhibition of actin polymerization at the TGN. Once PKD activity is terminated, synergistic actin polymerization is facilitated by non-S298-phosphorylated cortactin.

In addition to PKD activity, dimer formation between PKD2 and PKD3 isoforms was reported to coordinate secretion from the TGN (Bossard et al., 2007). We have previously shown that PKD1 and PKD2 can phosphorylate cortactin at S298 (Eiseler et al., 2010). Moreover, our data suggest that PKD3 can also phosphorylate endogenous cortactin (Fig. S2B). Thus, it is possible that PKD2 and PKD3 homo- or hetero-dimers at the TGN could also be implicated in the coordinated regulation of actin polymerization. However, this needs to be investigated in much more detail by determining actin polymerization upon abrogation of the PKD dimer formation in a follow-up study.

In our current manuscript, we were prompted to investigate the regulation of actin polymerization downstream of PKD2–cortactin at the TGN, since we have previously demonstrated an interaction of PKD2 with ARF1 and ARL1, vital governing GTPases during the vesicle biogenesis cycle (Eiseler et al., 2016). Once the lipid environment has been modified accordingly, active PKD needs to be inactivated to allow for the coordinated initiation of synergistic actin nucleation by the Arp2/3 complex. This is accomplished via active CDC42 (Fig. 3A–D; Fig. S2C,D). Whether cross-signaling by RhoGTPases and a link to microtubules, as suggested by Eisler et al. (2018), is associated with this process needs to be determined in future studies. In such a context, a putative link between CDC42 or RhoA activity and PKD2 activation as well as regulation through the ARF1 master switch for vesicle biogenesis (Dubois et al., 2005) will have to be further investigated in detail.

So far, it is also unknown how inactivation of PKD by CDC42 at the TGN is achieved at the molecular level. An intermediate mediator might be the lipid metabolite diacylglycerol (DAG). DAG is required for the recruitment of PKDs to TGN membranes, and co-activation of PKDs by novel protein kinase C (nPKC) upstream kinases (Wang, 2006). Formation of DAG at the TGN can be accomplished by different biosynthesis pathways, such as sphingomyelin synthase (SMS) (Subathra et al., 2011) or through phospholipase D1 (PLD1) (Ktistakis et al., 1995; Sarri et al., 2011). Phospholipase C β3 was also described to be implicated in DAG generation at the TGN (Diaz Anel, 2007). How the activity of the respective DAG biosynthesis pathways is linked to CDC42 activity is currently unclear, for example, the PLD1 isoform was reported to be regulated by several activators, including Rho family GTPases and PKC (Brown et al., 1995; Walker et al., 2000). Since CDC42 activation has also been shown to be DAG dependent (Vaughan et al., 2014), extensive research will be required to rigorously delineate biosynthesis pathways during PKD activation at the TGN downstream of CDC42.

In this study, we have measured actin turnover at the TGN by using LifeAct-Ruby FRAP (Figs 3E–H and 4), since LifeAct signals were considerably enriched at furin-GFP-positive structures (Fig. S8A,B). The enrichment of LifeAct signals at the TGN is in line with a previous study comparing different probes for F-actin

Journal of Cell Science (2019) 132, jcs232355. doi:10.1242/jcs.232355

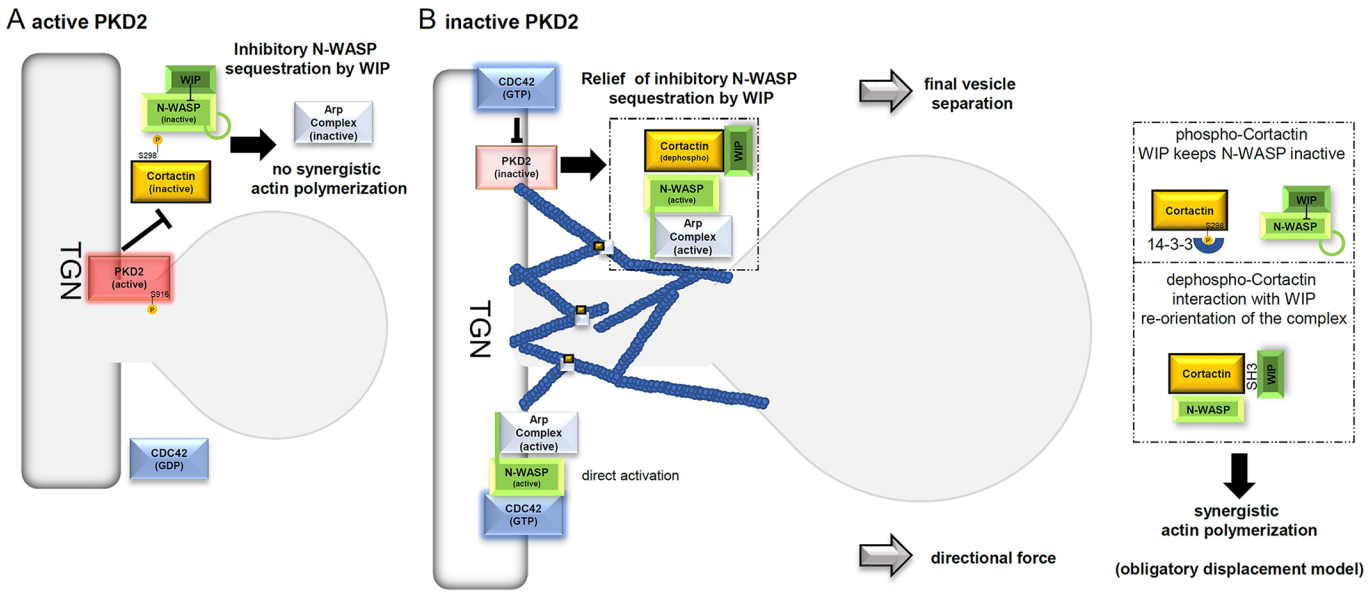

Fig. 8. Model for regulation of actin polymerization at the TGN. (A) Active PKD2 inhibits efficient actin polymerization during vesicle scission until a fission-compatible state is established. Phosphorylation of cortactin by PKD2 at S298 impairs the interaction between WIP and cortactin. WIP stabilizes the inactive autoinhibited conformation of N-WASP. This leads to an inhibition of synergistic actin polymerization as N-WASP cannot initiate activation of the Arp2/3 complex. (B) Active CDC42-GTP can directly activate N-WASP and disable a second level of inhibition, relieving N-WASP sequestration in the autoinhibited state by WIP. Active CDC42-GTP inactivates PKD2 and thereby shifts the balance to non-S298 phosphorylated-cortactin. Non-S298-phosphorylated-cortactin binds WIP and facilitates activation of N-WASP to initiate synergistic branching actin nucleation during transport carrier separation at the TGN.

live imaging at subcellular compartments (Belin et al., 2014). The use of LifeAct for FRAP analysis has been controversial owing to fast exchange rates on filaments (Belin et al., 2014; Riedl et al., 2008). However, in their experiments those authors have not investigated actin turnover at the Golgi compartment, where filaments are very short, transient and have very high turnover rates (Gurel et al., 2014), instead they measured stress fibers and lamellipodia. In our hands, FRAP experiments with LifeAct–Ruby were able to resolve differences in relative actin polymerization at the TGN. In contrast, in actin–Ruby FRAP experiments, even enhanced actin polymerization upon overexpression of constitutively active CDC42-Q61L was not detectable (data not shown). We suggest that this may be the result of insufficient enrichment at the TGN, as well as fast diffusion by actin monomers, which can also be observed by a fast, steep increase in fluorescence recovery (Fig. S8C,D).

Our data indicate that regulation of branching actin polymerization at the TGN is mediated by cortactin and its inhibitory phosphorylation via PKD2 in conjunction with N-WASP–WIP and the Arp complex. Thus, knockout of PKD2 resulted in enhanced steady-state actin polymerization at the TGN and this phenotype was reversed upon depletion of cortactin (Fig. 4C,D; Fig. S3G,H).

Nevertheless, we cannot exclude the possibility that, at least partially, other actin remodeling pathways controlled by PKD isoforms might be involved in regulating actin turnover at the TGN. One candidate is the slingshot–cofilin pathway, which generates barbed ends and monomers by severing filaments (DesMarais et al., 2005; Lorenz et al., 2004a). Furthermore, PKD1, slingshot and cofilin have been reported to generate Golgi outposts in neurites of neuronal cells and thus might regulate actin polymerization at the TGN (Quassollo et al., 2015). However, to generate forces that can drive separation of transport carriers from donor membranes, branching actin polymerization mediated by the Arp2/3 complex is required (Anitei et al., 2010). In addition to regulating synergistic actin polymerization with N-WASP, cortactin has been reported to stabilize actin branch junctions (Helgeson and Nolen, 2013), which may further facilitate vesicle release from TGN membranes. Moreover, *in vitro* and in invadopodia, cortactin has been demonstrated to directly interact with cofilin and inhibit its actin severing activity (Oser et al., 2009). Thus, it is not likely that both pathways contribute to actin polymerization at the same spatial location or at the same time.

Our current study is also consistent with the detailed description of molecular complexes involved in synergistic nucleation, proposed as an obligatory displacement model for WASP family NPFs (Helgeson and Nolen, 2013). Here, active N-WASP dimers initiate actin nucleation, which is then stalled, as long as N-WASP is occupying the Arp2/3 complex. Completion of the nucleation process was shown to require displacement of N-WASP from Arp2/3 by cortactin, freeing N-WASP for additional nucleation events (Helgeson and Nolen, 2013). Since we have shown enhanced synergistic nucleation for non-phosphorylatable cortactin-S298A in the presence of a VCA minimal fragment (Eiseler et al., 2010), it is likely that this cortactin mutant somehow affects displacement of WASP NPFs from the Apr2/3 complex. In contrast to the class I NPF N-WASP (Alekhina et al., 2017; Helgeson et al., 2014), cortactin is a weak class 2 NPF, unable to recruit actin monomers to the Arp2/3 complex (Helgeson and Nolen, 2013). Since recruitment of actin monomers is thought to induce conformational changes required for efficient nucleation (Helgeson and Nolen, 2013), monomer recruitment might be facilitated by interaction of the monomer-binding protein WIP with non-S298-phosphorylated cortactin during nucleation *in vivo* (Kinley et al., 2003). How these processes can be fully integrated in the obligatory displacement model (Helgeson and Nolen, 2013) remains to investigated.

Since binding of WIP to cortactin is dependent on its interaction with the cortactin SH3 domain (Kinley et al., 2003), we propose that

14-3-3 protein binding to the pS298 consensus site (Eiseler et al., 2010) induces conformational changes that inhibit efficient SH3-mediated interactions. This interpretation is in line with published data where SH3-dependent binding of interaction partners is masked or inhibited by 14-3-3-proteins bound to phosphorylated consensus motifs (Freeman and Morrison, 2011).

In summary, we here present a novel role for PKD2 and its phosphorylation of cortactin in the coordination and timing of synergistic actin nucleation at the TGN with the NPF N-WASP. We were further able to measure the respective changes in steady-state actin polymerization at the TGN and we also demonstrate an increase in constitutive secretion that is dependent on the same proteins (Fig. 8).

MATERIALS AND METHODS

Cell culture

HEK293T, HeLa and MCF-7 cells were recently acquired from ATCC. WI-38 cells were recently acquired from EACC via Sigma-Aldrich (Taufkirchen, Germany). NIH3T3 fibroblasts were kindly provided by Franz Oswald (University Clinics Ulm, Germany). The HUVEC endothelial cell line was kindly provided by Steffen Just (University Clinics Ulm, Germany). HEK293T, HeLa and MCF-7 cells were cultured in DMEM supplemented with 10% fetal calf serum (FCS) and 1% penicillin and streptomycin. WI-38 were cultured in DMEM with 15% FCS, 1% non-essential amino acids and 1% penicillin and streptomycin. HUVECs were cultured in MV2 endothelial growth medium with supplement and 1% penicillin and streptomycin (Promo Cell, Heidelberg, Germany). All cells were kept at 37°C in 5% CO_2. All cells were regular tested for contamination.

Reagents and antibodies

A full list of antibodies used in this study is available in Table S1. In Table S2 DNA expression vectors, lentiviral shRNAs and siRNAs are listed.

Generation of PKD2 and PKD3 CRISPR knockout cells

HeLa cells were acquired from the ATCC. PRKD2 isoform-selective CRISPR constructs containing gRNA and Cas9–GFP in a single expression vector (U6gRNA-Cas9-2A-GFP) were acquired from Sigma-Aldrich (Taufkirchen, Germany). The CRISPR construct gRNA sequence was designed as following: PRKD2, HS0000083056, target site, 5′-GCAGGAGGTTGGCCGACGTGGG-3′; PRKD3, HS0000321772, target site, 5′-GAGAGTATGTGGACGAATCTGG-3′. HeLa CRISPR lines were produced by transfecting cells with the respective CRISPR constructs using Lipofectamin 3000 (Thermo Fisher Scientific, St Leon-Rot, Germany). GFP-positive cells were subsequently transferred as single cells into 96-well culture plates by fluorescence-associated cell sorting (FACS). After 3 weeks of growth, cells from single clones were harvested, lysed as described in Eiseler et al. (2016) and analyzed for PKD isoform expression by western blotting. Positive hits were further verified by sequencing of PCR products from genomic DNA.

Cloning of cortactin mutants

The cortactinΔSH3 mutation was generated by PCR on pCR3.V62-Met-Flag-Cortactin template (Table S2) using forward primer 5′-ACGCGGA-ATTCAGGAAAGCTTCGACA-3′ and reverse primer 5′-AAGGGCCCC-TAGTTCTCGTACTCATCGTA-3′. The amplicon was inserted in pcDNA3 using EcoRI and ApaI. The cortactinΔSH3-S298A mutation was introduced by PCR with forward primer 5′-CTGGCCAAGCACGAGGCCCAGCA-AGAC-3′ and reverse primer 5′-GTCTTGCTGGGCCTCGTGCTTGGC-CAG-3′, pcDNA3-FLAG-CortactinΔSH3 was used as template.

Immunoprecipitation and western blot analysis

Samples were lysed in lysis buffer 1 (50 mM Tris-HCl pH 7.4, 150 mM NaCl, 5 mM $MgCl_2$, 1% Triton X-100) plus Complete protease® and PhosStop inhibitors® (Roche, Basel, Switzerland). Cell debris was removed by centrifugation (13,000 ***g*** for 10 min). Protein content in the lysate was measured using Bradford assay reagent (BioRad, Hercules, CA). For IP, the same amount of lysate was used for each condition and incubated with an appropriate antibody concentration for 2 h at 4°C. Protein-A–Sepharose beads (GE Healthcare Life Sciences, Chicago, IL) were added and further incubated for 2 h at 4°C. Samples were washed four times with 900 µl lysis buffer 1 and subjected to SDS-PAGE on 10% acrylamide gels. Samples were transferred onto nitrocellulose membranes. Blots were blocked with 2% BSA in TBS Tween-20. Primary antibodies were applied in blocking solution overnight at 4°C. The membranes were incubated with the appropriate secondary antibodies conjugated to horseradish peroxidase (HRP) for 1 to 2 hs at room temperature; signal was detected using SuperSignal West Dura reagent (Thermo Fisher Scientific). Quantitative analysis of western blots was performed by measuring integrated band densities using NIH ImageJ (National Institutes of Health, Bethesda, MD).

Treatment with CDC42 inhibitors

For western blot analysis, 5×10^5 HEK293T cells were seeded in six-well plates and processed as indicated. For confocal microscopy 8×10^4 HeLa cells were seeded on cover slips in 12-well plates. The next day, the growth medium was replaced with growth medium containing 10 µM ML141 (Sigma-Aldrich) or the same amount of DMSO. Cells were incubated for 1 h at 37°C, washed with PBS and either fixed for microscopy or lysed for western blotting. For FRAP experiments cells were prepared as described below. At 1 h prior to imaging medium was changed to Phenol Red-free medium containing 10 µM ML141, 5 µM Casin (Biotechne, Wiesbaden-Nordenstadt, Germany) or DMSO, respectively. ML141 was previously characterized by Surviladze et al. (2010) to have an IC_{50} for CDC42 of 0.2 µM, and for Rac1, Ras, Rab2a and Rab7 of greater than 100 µM (Surviladze et al., 2010). Casin (as Pirl1-related compound 2) was described to have an IC_{50} of 2 µM in an PIP2-stimulated actin polymerization assay (Peterson et al., 2006). Furthermore, casin was shown to inhibit CDC42 activity at 5 µM in murine hematopoietic stem cells (Florian et al., 2012).

CDC42 activation assay

The assay was performed with a CDC42 Activation Assay Biochem Kit from Cytoskeleton, Inc. (Denver, CO) according to the manufacture's manual. At 2 days prior to the assay, 15×10^5 WI-38 fibroblasts were seeded in 145 mm plates; 3.5 mg of cleared total cell lysate was used for the experiments. GTP-γS- and GDP-loaded CDC42 were used as respective control. Bound GTP-loaded CDC42 was analyzed by western blotting.

Confocal staining

For confocal imaging, cells were processed as described previously (Eiseler et al., 2016). In brief, 8×10^4 HeLa cells were seeded on sterilized 15×15 mm cover slips in 12-well plates. The next day cells were transfected using Lipofectamin 3000 (Thermo Fisher Scientific), treated with inhibitors and then fixed. Fixation was performed with 3.75% formaldehyde for 20 min at room temperature. Samples were permeabilized with 0.1% Triton X-100 in PBS for 30 s or 2 min. After blocking (5% FCS, 0.05% Tween-20 in PBS) for 20 min, samples were stained with primary antibody for 2 h at room temperature or overnight at 4°C. Samples were washed three times with PBS and secondary antibodies conjugated with an Alexa fluorophore were applied for 2 h at room temperature. Coverslips were mounted in Fluoromount-G (Thermo Fisher Scientific).

Acceptor-photobleach Förster resonance energy transfer resonance energy transfer

AB-FRET experiments were performed as described previously (Becher et al., 2017; Eiseler et al., 2016; Sroka et al., 2016). Cells were analyzed with a LSM710 confocal laser-scanning microscope (Zeiss, Jena, Germany) and TCS-SP8-HCS (Leica, Mannheim, Germany) equipped with HC PL APO 40×/1.30 Oil CS2, HC PL APO 40×/1.10 W CORR CS2 or HC PL APO 63×/1.20 W CORR CS2 immersion objectives. Images were acquired in sequential scan mode. Gain and offset were set in a way that all cellular structures were imaged within the linear range of detectors having no saturated pixels and black level background values. AB-FRET experiments were performed with transiently transfected HeLa cells, fixed, processed and stained as stated above. This method allows the determination of

protein–protein interactions indicated by an apparent molecular proximity below 10 nm (Becher et al., 2017; Eiseler et al., 2012, 2016; Gu et al., 2004; Kunkel and Newton, 2009; Oser et al., 2010; Sroka et al., 2016; Valente et al., 2012; Wille et al., 2014; Wouters et al., 1998; Zeug et al., 2012). The FRET acceptor in a region of interest (ROI) was bleached by an intensive laser line and increase in donor fluorescence, indicating FRET, was measured. AB-FRET measurements were carried out by acquiring pre- and post-bleach images of donor and acceptor using an automated time series. Donor dyes in cells were in all instances GFP-tagged proteins. Acceptors were labeled with Alexa-Fluor-568-conjugated antibodies or Phalloidin–Alexa-Fluor-568 (F-actin). As an internal threshold, 8-bit images (256 gray values) were used for recording raw data to only register substantial changes in fluorescence intensities as respective gray value changes. FRET values were acquired from at least three independent experiments. Cells were randomly sampled from slides. In experiments with ectopic transgenes, cells with very strong ectopic expression were not recorded to avoid artifacts. Image analysis was performed using NIH ImageJ. Quantitative FRET analysis was executed by calculating the mean percentage FRET and s.e.m. for each cell from non-thresholded raw data for equally sized sub-ROIs randomly placed on TGN-marker positive structures within the bleached region [$\%FRET=((Donor_{post}-Donor_{pre})/Donor_{post})\times100$]. Cells that failed to show FRET in the bleach-region were set to zero during analysis. Results are presented as scatter graphs with single percentage FRET values. Numbers on top of graphs indicate mean percentage FRET values and s.e.m. for all evaluated ROIs. Numbers in brackets indicate the number of cells with FRET in the bleach-region. Raw data for all AB-FRET experiments is provided in Table S3.

Huygens deconvolution

For Huygens deconvolution, images of the TGN from fixed cells embedded in Fluoromount G (Thermo Fisher Scientific; refractive index of 1.4), were acquired using a Leica TCS-SP8-HCS confocal laser-scanning microscope. Imaging conditions were set as follows: objective HC PL APO 63×/1.20 W CORR CS2; size: 4096×4096 or 2048×2048 pixels, pinhole: 0.6 AU, scan speed: 100–200 Hz bidirectional, *z*-stack encompassing several TGN sections (5–18) using a z-Galvo table. Image acquisition was performed with highly sensitive HyD GaAsP-hybrid detectors and the Huygens deconvolution software module. Subsequently, image stacks were loaded into the Huygens Essential Deconvolution software and processed by the Huygens optimized classical maximum likelihood estimation algorithm (CMLE).

FRAP imaging of LifeAct–Ruby or actin–Ruby fluorescence intensities at the TGN

HeLa cells (10^5) were seeded in 35 mm glass-bottom µ-dishes (Ibidi, Martinsried, Germany). The next day, cells were transfected with the indicated constructs using Lipofectamin 3000 (Thermo Fisher Scientific). To quantify actin polymerization at the TGN we recorded either LifeAct–RubyN143C or actin–Ruby fluorescence intensities at furin–GFP-positive TGN structures. Before the experiment, the growth medium was replaced with Phenol Red-free RPMI or DMEM plus 10% FCS and 1% penicillin-streptomycin. FRAP experiments were performed using a Leica TSC-SP8-HCS confocal laser scanning microscope using a tabletop incubator (Oko Labs, Ottaviano, NA, Italy) at 37°C and 5% CO_2. Images (512×512 pixels; scan speed 200 Hz) were acquired every second with a pinhole of 2 AU to compensate for dynamic movement of Golgi stacks during acquisition. Five pre-bleach images were acquired before bleaching of furin–GFP-positive TGN structures using a 561 nm laser line (AOTF 100%) to set a baseline for fluorescence intensity measurements at the TGN. Subsequently, LifeAct–RubyN143C or actin–Ruby fluorescence intensities, respectively, were recorded for 130 s. Mean of ROI fluorescence intensities at the TGN were determined using detection masks generated around the furin–GFP signal.

Proximity-ligation-assay microscopy

HeLa cells (3×10^4) were seeded on sterilized 12 mm diameter coverslips in 24-well plates. The next day cells were transfected with a plasmid encoding for Furrin-GFP using Lipofectamin 3000 (Thermo Fisher Scientific). The following day samples were fixed for 20 min with 3.7% PFA at room temperature. Cells were permeabilized with 0.1% Triton X-100 in PBS for 2 min. PLA staining was performed according to manufactures protocol with Duolink In Situ Red Starter Kit Mouse/Rabbit (Sigma-Aldrich).

N-WASP FRET biosensor assays in total cell lysates

The extent of N-WASP activity was determined by quantifying the presence of open, unfolded N-WASP conformations using a CFP–N-WASP–YFP FRET activity sensor that loses Förster energy transfer after relieving autoinhibition (Lorenz et al., 2004b; Oser et al., 2009). The sensor was initially characterized by Lorenz et al. (2004b). HEK293T (1.5×10^5) cells were co-transfected with sensor and the indicated constructs (ratio: 1 to 3) in a 12-well plate format. After 24 h cells were lysed in 100 µl FRET lysis buffer (20 mM Tris-HCl pH 7.4, 100 mM NaCl, 5 mM $MgCl_2$ and 0.5% Triton X-100) with Complete® protease and PhosStop® inhibitors (Roche) for 20 min. After lysates have been cleared by centrifugation 80 µl of cleared lysates were measured in a black non-binding 96-well plate using a Tecan M-200 Pro (Tecan, Halver, Germany) plate reader (CFP, Ex: 433 nm, Em: 475 nm; FRET, Ex 433 nm, Em: 527 nm). FRET was calculated by generating mean CFP:FRET ratios for n=12 transfected samples. Expression of transgenes was verified by western blotting.

Perinuclear N-WASP FRET sensor measurements in MCF-7 cells

The CFP–N-WASP–YFP FRET activity sensor was co-transfected with the indicated constructs in MCF-7 cells on 35 mm µ-dishes (Ibidi, Martinsried, Germany). After 24 h, cells were serum-starved in Phenol Red-free RPMI medium for 4 h and then subjected to live imaging using a LSM710 confocal laser scanning microscope (Zeiss, Jena, Germany) at 37°C and 5% CO_2 employing a 63× high NA objective. Images were acquired in ROI scan mode centered on the perinuclear region of a cell with enriched presence of the N-WASP sensor (512×512 pixels; pixel dwell: 6.3 µs; Ex: 405 nm laser, Em: CFP: 470-501 nm; Em: FRET: 524-550 nm, 1 frame/s; pinhole 30 µm to compensate for dynamic Golgi movements). After 60 s, cells were stimulated with 100 ng/ml Heregulin (PeproTech, London, UK). Fluorescence intensities in the clipped scan ROIs were analyzed by NIH ImageJ and presented as CFP:FRET ratios.

HRP secretion assay

To determine the extent of constitutive secretion, we measured release of the artificial cargo HRP (Cruz-Garcia et al., 2013; Fugmann et al., 2007) from HEK293T cells. HEK293T cells were modified either by transduction with lentiviruses coding for shRNAs (Table S2) to generate semi-stable knockdown cell lines upon selection with puromycin 6 µg/ml for 1 week or by transiently co-transfecting cells with the indicated DNA expression constructs and HRP as well as siRNAs (ratio: 3 to 1) in a 6-well format. After transfection of siRNAs, cells were incubated for 48 h. Subsequently, cells were carefully washed three times and incubated with 600 µl of serum-free, Phenol Red-free RMPI medium for 4 h. Supernatants were harvested, cleared and 5 µl were incubated with 200 µl freshly prepared ECL solution (Luminol 224 mg, Coumaric acid 37.1 mg, 0.05% H_2O_2 in 100 ml 50 mM Tris-HCk pH 8.0) in white non-binding 96-well plates for 5 min to reach equilibration. The presence of HRP in cell culture supernatants was subsequently detected by measuring luminescence using a Tecan M-200 Pro plate reader. In general, five or six independent experiments with three technical replicas were quantified.

Statistical analyses

Statistical analyses were performed using Prism software version 6 or 8 for Windows (GraphPad Software, San Diego, CA). Graphs depict mean±s.e.m. for all conditions. Normality was tested with a D'Agostino and Pearson omnibus test. Statistical significance is indicated by asterisks (ns, not significant; *P<0.05; **P<0.01; ***P<0.001; ****P<0.0001).

Acknowledgements

The authors want to acknowledge use of the Imaging Core Facility for 'Multiphoton and Confocal Microscopy' and FACS Core Facility at Ulm University. We thank Ralf Kemkemer, Franz Oswald, Johan van Lint, Steffen Just and Angelika Hausser for providing valuable research reagents. We thank Claudia Ruhland, Edith Glass and Susanne Fluhr for excellent technical assistance.

Competing interests
The authors declare no competing or financial interests.

Author contributions
Conceptualization: T.E.; Formal analysis: F.W., A.B., T. Seibold, T. Seufferlein, T.E.; Investigation: F.W., A.B., T. Seibold, T.E.; Resources: T. Seufferlein, T.E.; Writing - original draft: F.W., A.B., T. Seibold, T. Seufferlein, T.E.; Writing - review & editing: T.E.;Visualization: F.W., T.E.; Supervision: T. Seufferlein, T.E.; Project administration: T.E.; Funding acquisition: T. Seufferlein, T.E.

Funding
The project was funded by the Deutsche Forschungsgemeinschaft (grant EI792/7-1).

Supplementary information
Supplementary information available online at
http://jcs.biologists.org/lookup/doi/10.1242/jcs.232355.supplemental

References

Alekhina, O., Burstein, E. and Billadeau, D. D. (2017). Cellular functions of WASP family proteins at a glance. *J. Cell Sci.* **130**, 2235-2241. doi:10.1242/jcs.199570

Anitei, M., Stange, C., Parshina, I., Baust, T., Schenck, A., Raposo, G., Kirchhausen, T. and Hoflack, B. (2010). Protein complexes containing CYFIP/Sra/PIR121 coordinate Arf1 and Rac1 signalling during clathrin-AP-1-coated carrier biogenesis at the TGN. *Nat. Cell Biol.* **12**, 330-340. doi:10.1038/ncb2034

Baron, C. L. and Malhotra, V. (2002). Role of diacylglycerol in PKD recruitment to the TGN and protein transport to the plasma membrane. *Science* **295**, 325-328. doi:10.1126/science.1066759

Becher, A., Eiseler, T., Porzner, M., Walther, P., Keil, R., Bobrovich, S., Hatzfeld, M. and Seufferlein, T. (2017). The armadillo protein p0071 controls KIF3 motor transport. *J. Cell Sci.* **130**, 3374-3387. doi:10.1242/jcs.200170

Belin, B. J., Goins, L. M. and Mullins, R. D. (2014). Comparative analysis of tools for live cell imaging of actin network architecture. *Bioarchitecture* **4**, 189-202. doi:10.1080/19490992.2014.1047714

Bhattacharya, K., Swaminathan, K., Peche, V. S., Clemen, C. S., Knyphausen, P., Lammers, M., Noegel, A. A. and Rastetter, R. H. (2016). Novel Coronin7 interactions with Cdc42 and N-WASP regulate actin organization and Golgi morphology. *Sci. Rep.* **6**, 25411. doi:10.1038/srep25411

Bossard, C., Bresson, D., Polishchuk, R. S. and Malhotra, V. (2007). Dimeric PKD regulates membrane fission to form transport carriers at the TGN. *J. Cell Biol.* **179**, 1123-1131. doi:10.1083/jcb.200703166

Brown, H. A., Gutowski, S., Kahn, R. A. and Sternweis, P. C. (1995). Partial purification and characterization of Arf-sensitive phospholipase D from porcine brain. *J. Biol. Chem.* **270**, 14935-14943. doi:10.1074/jbc.270.25.14935

Campellone, K. G., Siripala, A. D., Leong, J. M. and Welch, M. D. (2012). Membrane-deforming proteins play distinct roles in actin pedestal biogenesis by enterohemorrhagic Escherichia coli. *J. Biol. Chem.* **287**, 20613-20624. doi:10.1074/jbc.M112.363473

Cao, H., Weller, S., Orth, J. D., Chen, J., Huang, B., Chen, J.-L., Stamnes, M. and McNiven, M. A. (2005). Actin and Arf1-dependent recruitment of a cortactin-dynamin complex to the Golgi regulates post-Golgi transport. *Nat. Cell Biol.* **7**, 483-492. doi:10.1038/ncb1246

Cruz-Garcia, D., Ortega-Bellido, M., Scarpa, M., Villeneuve, J., Jovic, M., Porzner, M., Balla, T., Seufferlein, T. and Malhotra, V. (2013). Recruitment of arfaptins to the trans-Golgi network by PI(4)P and their involvement in cargo export. *EMBO J.* **32**, 1717-1729. doi:10.1038/emboj.2013.116

DesMarais, V., Ghosh, M., Eddy, R. and Condeelis, J. (2005). Cofilin takes the lead. *J. Cell Sci.* **118**, 19-26. doi:10.1242/jcs.01631

Diaz Anel, A. M. (2007). Phospholipase C beta3 is a key component in the Gbetagamma/PKCeta/PKD-mediated regulation of trans-Golgi network to plasma membrane transport. *Biochem. J.* **406**, 157-165. doi:10.1042/BJ20070359

Döppler, H., Bastea, L. I., Eiseler, T. and Storz, P. (2013). Neuregulin mediates F-actin-driven cell migration through inhibition of protein kinase D1 via Rac1 protein. *J. Biol. Chem.* **288**, 455-465. doi:10.1074/jbc.M112.397448

Dubois, T. and Chavrier, P. (2005). [ARHGAP10, a novel RhoGAP at the cross-road between ARF1 and Cdc42 pathways, regulates Arp2/3 complex and actin dynamics on Golgi membranes]. *Med. Sci. (Paris)* **21**, 692-694. doi:10.1051/medsci/2005218-9692

Dubois, T., Paléotti, O., Mironov, A. A., Fraisier, V., Stradal, T. E. B., De Matteis, M. A., Franco, M. and Chavrier, P. (2005). Golgi-localized GAP for Cdc42 functions downstream of ARF1 to control Arp2/3 complex and F-actin dynamics. *Nat. Cell Biol.* **7**, 353-364. doi:10.1038/ncb1244

Egea, G., Lázaro-Diéguez, F. and Vilella, M. (2006). Actin dynamics at the Golgi complex in mammalian cells. *Curr. Opin. Cell Biol.* **18**, 168-178. doi:10.1016/j.ceb.2006.02.007

Eiseler, T., Hausser, A., De Kimpe, L., Van Lint, J. and Pfizenmaier, K. (2010). Protein kinase D controls actin polymerization and cell motility through phosphorylation of cortactin. *J. Biol. Chem.* **285**, 18672-18683. doi:10.1074/jbc.M109.093880

Eiseler, T., Köhler, C., Nimmagadda, S. C., Jamali, A., Funk, N., Joodi, G., Storz, P. and Seufferlein, T. (2012). Protein kinase D1 mediates anchorage-dependent and -independent growth of tumor cells via the zinc finger transcription factor Snail1. *J. Biol. Chem.* **287**, 32367-32380. doi:10.1074/jbc.M112.370999

Eiseler, T., Wille, C., Koehler, C., Illing, A. and Seufferlein, T. (2016). Protein kinase D2 assembles a multiprotein complex at the trans-golgi network to regulate matrix metalloproteinase secretion. *J. Biol. Chem.* **291**, 462-477. doi:10.1074/jbc.M115.673582

Eisler, S. A., Curado, F., Link, G., Schulz, S., Noack, M., Steinke, M., Olayioye, M. A. and Hausser, A. (2018). A Rho signaling network links microtubules to PKD controlled carrier transport to focal adhesions. *eLife* **7**, e35907. doi:10.7554/eLife.35907

Estrada, L., Caron, E. and Gorski, J. L. (2001). Fgd1, the Cdc42 guanine nucleotide exchange factor responsible for faciogenital dysplasia, is localized to the subcortical actin cytoskeleton and Golgi membrane. *Hum. Mol. Genet.* **10**, 485-495. doi:10.1093/hmg/10.5.485

Florian, M. C., Dörr, K., Niebel, A., Daria, D., Schrezenmeier, H., Rojewski, M., Filippi, M.-D., Hasenberg, A., Gunzer, M., Scharffetter-Kochanek, K. et al. (2012). Cdc42 activity regulates hematopoietic stem cell aging and rejuvenation. *Cell Stem Cell* **10**, 520-530. doi:10.1016/j.stem.2012.04.007

Freeman, A. K. and Morrison, D. K. (2011). 14-3-3 Proteins: diverse functions in cell proliferation and cancer progression. *Semin. Cell Dev. Biol.* **22**, 681-687. doi:10.1016/j.semcdb.2011.08.009

Fugmann, T., Hausser, A., Schöffler, P., Schmid, S., Pfizenmaier, K. and Olayioye, M. A. (2007). Regulation of secretory transport by protein kinase D-mediated phosphorylation of the ceramide transfer protein. *J. Cell Biol.* **178**, 15-22. doi:10.1083/jcb.200612017

Ghanekar, Y. and Lowe, M. (2005). Protein kinase D: activation for Golgi carrier formation. *Trends Cell Biol.* **15**, 511-514. doi:10.1016/j.tcb.2005.08.001

Gu, Y., Di, W. L., Kelsell, D. P. and Zicha, D. (2004). Quantitative fluorescence resonance energy transfer (FRET) measurement with acceptor photobleaching and spectral unmixing. *J. Microsc.* **215**, 162-173. doi:10.1111/j.0022-2720.2004.01365.x

Gurel, P. S., Hatch, A. L. and Higgs, H. N. (2014). Connecting the cytoskeleton to the endoplasmic reticulum and Golgi. *Curr. Biol.* **24**, R660-R672. doi:10.1016/j.cub.2014.05.033

Hausser, A., Storz, P., Märtens, S., Link, G., Toker, A. and Pfizenmaier, K. (2005). Protein kinase D regulates vesicular transport by phosphorylating and activating phosphatidylinositol-4 kinase IIIbeta at the Golgi complex. *Nat. Cell Biol.* **7**, 880-886. doi:10.1038/ncb1289

Helgeson, L. A. and Nolen, B. J. (2013). Mechanism of synergistic activation of Arp2/3 complex by cortactin and N-WASP. *eLife* **2**, e00884. doi:10.7554/eLife.00884

Helgeson, L. A., Prendergast, J. G., Wagner, A. R., Rodnick-Smith, M. and Nolen, B. J. (2014). Interactions with actin monomers, actin filaments, and Arp2/3 complex define the roles of WASP family proteins and cortactin in coordinately regulating branched actin networks. *J. Biol. Chem.* **289**, 28856-28869. doi:10.1074/jbc.M114.587527

Higgs, H. N. and Pollard, T. D. (2001). Regulation of actin filament network formation through ARP2/3 complex: activation by a diverse array of proteins. *Annu. Rev. Biochem.* **70**, 649-676. doi:10.1146/annurev.biochem.70.1.649

Ho, H.-Y. H., Rohatgi, R., Lebensohn, A. M., Le Ma, A. M., Li, J., Gygi, S. P. and Kirschner, M. W. (2004). Toca-1 mediates Cdc42-dependent actin nucleation by activating the N-WASP-WIP complex. *Cell* **118**, 203-216. doi:10.1016/j.cell.2004.06.027

Hong, L., Kenney, S. R., Phillips, G. K., Simpson, D., Schroeder, C. E., Nöth, J., Romero, E., Swanson, S., Waller, A., Strouse, J. J. et al. (2013). Characterization of a Cdc42 protein inhibitor and its use as a molecular probe. *J. Biol. Chem.* **288**, 8531-8543. doi:10.1074/jbc.M112.435941

Kessels, M. M. and Qualmann, B. (2005). Extending the court for cortactin: from the cortex to the Golgi. *Nat. Cell Biol.* **7**, 448-449. doi:10.1038/ncb0505-448

Kienzle, C., Basnet, N., Crevenna, A. H., Beck, G., Habermann, B., Mizuno, N. and von Blume, J. (2014). Cofilin recruits F-actin to SPCA1 and promotes Ca2+-mediated secretory cargo sorting. *J. Cell Biol.* **206**, 635-654. doi:10.1083/jcb.201311052

Kinley, A. W., Weed, S. A., Weaver, A. M., Karginov, A. V., Bissonette, E., Cooper, J. A. and Parsons, J. T. (2003). Cortactin interacts with WIP in regulating Arp2/3 activation and membrane protrusion. *Curr. Biol.* **13**, 384-393. doi:10.1016/S0960-9822(03)00107-6

Kowalski, J. R., Egile, C., Gil, S., Snapper, S. B., Li, R. and Thomas, S. M. (2005). Cortactin regulates cell migration through activation of N-WASP. *J. Cell Sci.* **118**, 79-87. doi:10.1242/jcs.01586

Ktistakis, N. T., Brown, H. A., Sternweis, P. C. and Roth, M. G. (1995). Phospholipase D is present on Golgi-enriched membranes and its activation by ADP ribosylation factor is sensitive to brefeldin A. *Proc. Natl. Acad. Sci. USA* **92**, 4952-4956. doi:10.1073/pnas.92.11.4952

Kunkel, M. T. and Newton, A. C. (2009). Spatiotemporal dynamics of kinase signaling visualized by targeted reporters. *Curr. Protoc. Chem. Biol.* **1**, 17-18. doi:10.1002/9780470559277.ch090106

Liljedahl, M., Maeda, Y., Colanzi, A., Ayala, I., Van Lint, J. and Malhotra, V. (2001). Protein kinase D regulates the fission of cell surface destined transport

carriers from the trans-Golgi network. *Cell* **104**, 409-420. doi:10.1016/S0092-8674(01)00228-8

Lorenz, M., DesMarais, V., Macaluso, F., Singer, R. H. and Condeelis, J. (2004a). Measurement of barbed ends, actin polymerization, and motility in live carcinoma cells after growth factor stimulation. *Cell Motil. Cytoskeleton* **57**, 207-217. doi:10.1002/cm.10171

Lorenz, M., Yamaguchi, H., Wang, Y., Singer, R. H. and Condeelis, J. (2004b). Imaging sites of N-wasp activity in lamellipodia and invadopodia of carcinoma cells. *Curr. Biol.* **14**, 697-703. doi:10.1016/j.cub.2004.04.008

Luna, A., Matas, O. B., Martínez-Menárguez, J. A., Mato, E., Durán, J. M., Ballesta, J., Way, M. and Egea, G. (2002). Regulation of protein transport from the Golgi complex to the endoplasmic reticulum by CDC42 and N-WASP. *Mol. Biol. Cell* **13**, 866-879. doi:10.1091/mbc.01-12-0579

Mackintosh, C. (2004). Dynamic interactions between 14-3-3 proteins and phosphoproteins regulate diverse cellular processes. *Biochem. J.* **381**, 329-342. doi:10.1042/BJ20031332

Malhotra, V. and Campelo, F. (2011). PKD regulates membrane fission to generate TGN to cell surface transport carriers. *Cold Spring Harb. Perspect. Biol.* **3**, a005280. doi:10.1101/cshperspect.a005280

Matas, O. B., Martínez-Menárguez, J. A. and Egea, G. (2004). Association of Cdc42/N-WASP/Arp2/3 signaling pathway with Golgi membranes. *Traffic* **5**, 838-846. doi:10.1111/j.1600-0854.2004.00225.x

Ménétrey, J., Perderiset, M., Cicolari, J., Dubois, T., Elkhatib, N., El Khadali, F., Franco, M., Chavrier, P. and Houdusse, A. (2007). Structural basis for ARF1-mediated recruitment of ARHGAP21 to Golgi membranes. *EMBO J.* **26**, 1953-1962. doi:10.1038/sj.emboj.7601634

Mizutani, K., Miki, H., He, H., Maruta, H. and Takenawa, T. (2002). Essential role of neural Wiskott-Aldrich syndrome protein in podosome formation and degradation of extracellular matrix in Src-transformed fibroblasts. 62, 669-674.

Mizutani, K., Suetsugu, S. and Takenawa, T. (2004). FBP11 regulates nuclear localization of N-WASP and inhibits N-WASP-dependent microspike formation. *Biochem. Biophys. Res. Commun.* **313**, 468-474. doi:10.1016/j.bbrc.2003.11.139

Moreau, V., Frischknecht, F., Reckmann, I., Vincentelli, R., Rabut, G., Stewart, D. and Way, M. (2000). A complex of N-WASP and WIP integrates signalling cascades that lead to actin polymerization. *Nat. Cell Biol.* **2**, 441-448. doi:10.1038/35017080

Musch, A., Cohen, D., Kreitzer, G. and Rodriguez-Boulan, E. (2001). cdc42 regulates the exit of apical and basolateral proteins from the trans-Golgi network. *EMBO J.* **20**, 2171-2179. doi:10.1093/emboj/20.9.2171

Muslin, A. J. and Xing, H. (2000). 14-3-3 proteins: regulation of subcellular localization by molecular interference. *Cell. Signal.* **12**, 703-709. doi:10.1016/S0898-6568(00)00131-5

Oser, M., Yamaguchi, H., Mader, C. C., Bravo-Cordero, J. J., Arias, M., Chen, X., Desmarais, V., van Rheenen, J., Koleske, A. J. and Condeelis, J. (2009). Cortactin regulates cofilin and N-WASp activities to control the stages of invadopodium assembly and maturation. *J. Cell Biol.* **186**, 571-587. doi:10.1083/jcb.200812176

Oser, M., Mader, C. C., Gil-Henn, H., Magalhaes, M., Bravo-Cordero, J. J., Koleske, A. J. and Condeelis, J. (2010). Specific tyrosine phosphorylation sites on cortactin regulate Nck1-dependent actin polymerization in invadopodia. *J. Cell Sci.* **123**, 3662-3673. doi:10.1242/jcs.068163

Papayannopoulos, V., Co, C., Prehoda, K. E., Snapper, S., Taunton, J. and Lim, W. A. (2005). A polybasic motif allows N-WASP to act as a sensor of PIP(2) density. *Mol. Cell* **17**, 181-191. doi:10.1016/j.molcel.2004.11.054

Peterson, J. R., Lebensohn, A. M., Pelish, H. E. and Kirschner, M. W. (2006). Biochemical suppression of small-molecule inhibitors: a strategy to identify inhibitor targets and signaling pathway components. *Chem. Biol.* **13**, 443-452. doi:10.1016/j.chembiol.2006.02.009

Pfeffer, S. R. (2010). Recent advances in understanding Golgi biogenesis. *F1000 Biol. Rep.* **2**, 32. doi:10.3410/B2-32

Prehoda, K. E., Scott, J. A., Mullins, R. D. and Lim, W. A. (2000). Integration of multiple signals through cooperative regulation of the N-WASP-Arp2/3 complex. *Science* **290**, 801-806. doi:10.1126/science.290.5492.801

Pusapati, G. V., Krndija, D., Armacki, M., von Wichert, G., von Blume, J., Malhotra, V., Adler, G. and Seufferlein, T. (2010). Role of the second cysteine-rich domain and Pro275 in protein kinase D2 interaction with ADP-ribosylation factor 1, trans-Golgi network recruitment, and protein transport. *Mol. Biol. Cell* **21**, 1011-1022. doi:10.1091/mbc.e09-09-0814

Qualmann, B., Kessels, M. M. and Kelly, R. B. (2000). Molecular links between endocytosis and the actin cytoskeleton. *J. Cell Biol.* **150**, F111-F116. doi:10.1083/jcb.150.5.F111

Quassollo, G., Wojnacki, J., Salas, D. A., Gastaldi, L., Marzolo, M. P., Conde, C., Bisbal, M., Couve, A. and Cáceres, A. (2015). A RhoA signaling pathway regulates dendritic golgi outpost formation. *Curr. Biol.* **25**, 971-982. doi:10.1016/j.cub.2015.01.075

Ramesh, N. and Geha, R. (2009). Recent advances in the biology of WASP and WIP. *Immunol. Res.* **44**, 99-111. doi:10.1007/s12026-008-8086-1

Riedl, J., Crevenna, A. H., Kessenbrock, K., Yu, J. H., Neukirchen, D., Bista, M., Bradke, F., Jenne, D., Holak, T. A., Werb, Z. et al. (2008). Lifeact: a versatile marker to visualize F-actin. *Nat. Methods* **5**, 605-607. doi:10.1038/nmeth.1220

Rohatgi, R., Ho, H.-H. and Kirschner, M. W. (2000). Mechanism of N-WASP activation by CDC42 and phosphatidylinositol 4, 5-bisphosphate. *J. Cell Biol.* **150**, 1299-1310. doi:10.1083/jcb.150.6.1299

Sarri, E., Sicart, A., Lázaro-Diéguez, F. and Egea, G. (2011). Phospholipid synthesis participates in the regulation of diacylglycerol required for membrane trafficking at the Golgi complex. *J. Biol. Chem.* **286**, 28632-28643. doi:10.1074/jbc.M111.267534

Scaplehorn, N., Holmström, A., Moreau, V., Frischknecht, F., Reckmann, I. and Way, M. (2002). Grb2 and Nck act cooperatively to promote actin-based motility of vaccinia virus. *Curr. Biol.* **12**, 740-745. doi:10.1016/S0960-9822(02)00812-6

Schnoor, M., Stradal, T. E. and Rottner, K. (2018). Cortactin: cell functions of a multifaceted actin-binding protein. *Trends Cell Biol.* **28**, 79-98. doi:10.1016/j.tcb.2017.10.009

Shin, N., Ahn, N., Chang-Ileto, B., Park, J., Takei, K., Ahn, S.-G., Kim, S.-A., Di Paolo, G. and Chang, S. (2008). SNX9 regulates tubular invagination of the plasma membrane through interaction with actin cytoskeleton and dynamin 2. *J. Cell Sci.* **121**, 1252-1263. doi:10.1242/jcs.016709

Smythe, E. and Ayscough, K. R. (2006). Actin regulation in endocytosis. *J. Cell Sci.* **119**, 4589-4598. doi:10.1242/jcs.03247

Sroka, R., Van Lint, J., Katz, S.-F., Schneider, M. R., Kleger, A., Paschke, S., Seufferlein, T. and Eiseler, T. (2016). Cortactin is a scaffolding platform for the E-cadherin adhesion complex and is regulated by protein kinase D1 phosphorylation. *J. Cell Sci.* **129**, 2416-2429. doi:10.1242/jcs.184721

Stamnes, M. (2002). Regulating the actin cytoskeleton during vesicular transport. *Curr. Opin. Cell Biol.* **14**, 428-433. doi:10.1016/S0955-0674(02)00349-6

Subathra, M., Qureshi, A. and Luberto, C. (2011). Sphingomyelin synthases regulate protein trafficking and secretion. *PLoS ONE* **6**, e23644. doi:10.1371/journal.pone.0023644

Suetsugu, S. and Takenawa, T. (2003). Translocation of N-WASP by nuclear localization and export signals into the nucleus modulates expression of HSP90. *J. Biol. Chem.* **278**, 42515-42523. doi:10.1074/jbc.M302177200

Surviladze, Z., Waller, A., Strouse, J. J., Bologa, C., Ursu, O., Salas, V., Parkinson, J. F., Phillips, G. K., Romero, E., Wandinger-Ness, A. et al. (2010). A potent and selective inhibitor of Cdc42 GTPase. In *Probe Reports from the NIH Molecular Libraries Program*. Bethesda, MD.

Takano, K., Toyooka, K. and Suetsugu, S. (2008). EFC/F-BAR proteins and the N-WASP-WIP complex induce membrane curvature-dependent actin polymerization. *EMBO J.* **27**, 2817-2828. doi:10.1038/emboj.2008.216

Ti, S. C., Jurgenson, C. T., Nolen, B. J. and Pollard, T. D. (2011). Structural and biochemical characterization of two binding sites for nucleation-promoting factor WASp-VCA on Arp2/3 complex. *Proc. Natl. Acad. Sci. USA* **108**, E463-E471. doi:10.1073/pnas.1100125108

Tomasevic, N., Jia, Z., Russell, A., Fujii, T., Hartman, J. J., Clancy, S., Wang, M., Beraud, C., Wood, K. W. and Sakowicz, R. (2007). Differential regulation of WASP and N-WASP by Cdc42, Rac1, Nck, and PI(4,5)P2. *Biochemistry* **46**, 3494-3502. doi:10.1021/bi062152y

Valderrama, F., Babià, T., Ayala, I., Kok, J. W., Renau-Piqueras, J. and Egea, G. (1998). Actin microfilaments are essential for the cytological positioning and morphology of the Golgi complex. *Eur. J. Cell Biol.* **76**, 9-17. doi:10.1016/S0171-9335(98)80012-5

Valderrama, F., Luna, A., Babia, T., Martinez-Menarguez, J. A., Ballesta, J., Barth, H., Chaponnier, C., Renau-Piqueras, J. and Egea, G. (2000). The golgi-associated COPI-coated buds and vesicles contain beta/gamma -actin. *Proc. Natl. Acad. Sci. USA* **97**, 1560-1565. doi:10.1073/pnas.97.4.1560

Valderrama, F., Duran, J. M., Babia, T., Barth, H., Renau-Piqueras, J. and Egea, G. (2001). Actin microfilaments facilitate the retrograde transport from the Golgi complex to the endoplasmic reticulum in mammalian cells. *Traffic* **2**, 717-726. doi:10.1034/j.1600-0854.2001.21006.x

Valente, C., Turacchio, G., Mariggiò, S., Pagliuso, A., Gaibisso, R., Di Tullio, G., Santoro, M., Formiggini, F., Spano, S., Piccini, D. et al. (2012). A 14-3-3gamma dimer-based scaffold bridges CtBP1-S/BARS to PI(4)KIIIbeta to regulate post-Golgi carrier formation. *Nat. Cell Biol.* **14**, 343-354. doi:10.1038/ncb2445

Vaughan, E. M., You, J.-S., Elsie Yu, H.-Y., Lasek, A., Vitale, N., Hornberger, T. A. and Bement, W. M. (2014). Lipid domain-dependent regulation of single-cell wound repair. *Mol. Biol. Cell* **25**, 1867-1876. doi:10.1091/mbc.e14-03-0839

Walker, S. J., Wu, W.-J., Cerione, R. A. and Brown, H. A. (2000). Activation of phospholipase D1 by Cdc42 requires the Rho insert region. *J. Biol. Chem.* **275**, 15665-15668. doi:10.1074/jbc.M000076200

Wang, Q. J. (2006). PKD at the crossroads of DAG and PKC signaling. *Trends Pharmacol. Sci.* **27**, 317-323. doi:10.1016/j.tips.2006.04.003

Wille, C., Köhler, C., Armacki, M., Jamali, A., Gössele, U., Pfizenmaier, K., Seufferlein, T. and Eiseler, T. (2014). Protein kinase D2 induces invasion of pancreatic cancer cells by regulating matrix metalloproteinases. *Mol. Biol. Cell* **25**, 324-336. doi:10.1091/mbc.e13-06-0334

Wille, C., Eiseler, T., Langenberger, S.-T., Richter, J., Mizuno, K., Radermacher, P., Knippschild, U., Huber-Lang, M., Seufferlein, T. and Paschke, S. (2018). PKD regulates actin polymerization, neutrophil deformability, and transendothelial migration in response to fMLP and trauma. *J. Leukoc. Biol.* **104**, 615-630. doi:10.1002/JLB.4A0617-251RR

Wouters, F. S., Bastiaens, P. I., Wirtz, K. W. and Jovin, T. M. (1998). FRET microscopy demonstrates molecular association of non-specific lipid transfer protein (nsL-TP) with fatty acid oxidation enzymes in peroxisomes. *EMBO J.* **17**, 7179-7189. doi:10.1093/emboj/17.24.7179

Wu, X., Suetsugu, S., Cooper, L. A., Takenawa, T. and Guan, J.-L. (2004). Focal adhesion kinase regulation of N-WASP subcellular localization and function. *J. Biol. Chem.* **279**, 9565-9576. doi:10.1074/jbc.M310739200

Yeaman, C., Ayala, M. I., Wright, J. R., Bard, F., Bossard, C., Ang, A., Maeda, Y., Seufferlein, T., Mellman, I., Nelson, W. J. et al. (2004). Protein kinase D regulates basolateral membrane protein exit from trans-Golgi network. *Nat. Cell Biol.* **6**, 106-112. doi:10.1038/ncb1090

Zeug, A., Woehler, A., Neher, E. and Ponimaskin, E. G. (2012). Quantitative intensity-based FRET approaches–a comparative snapshot. *Biophys. J.* **103**, 1821-1827. doi:10.1016/j.bpj.2012.09.031

Supplemental Information

Figure S1

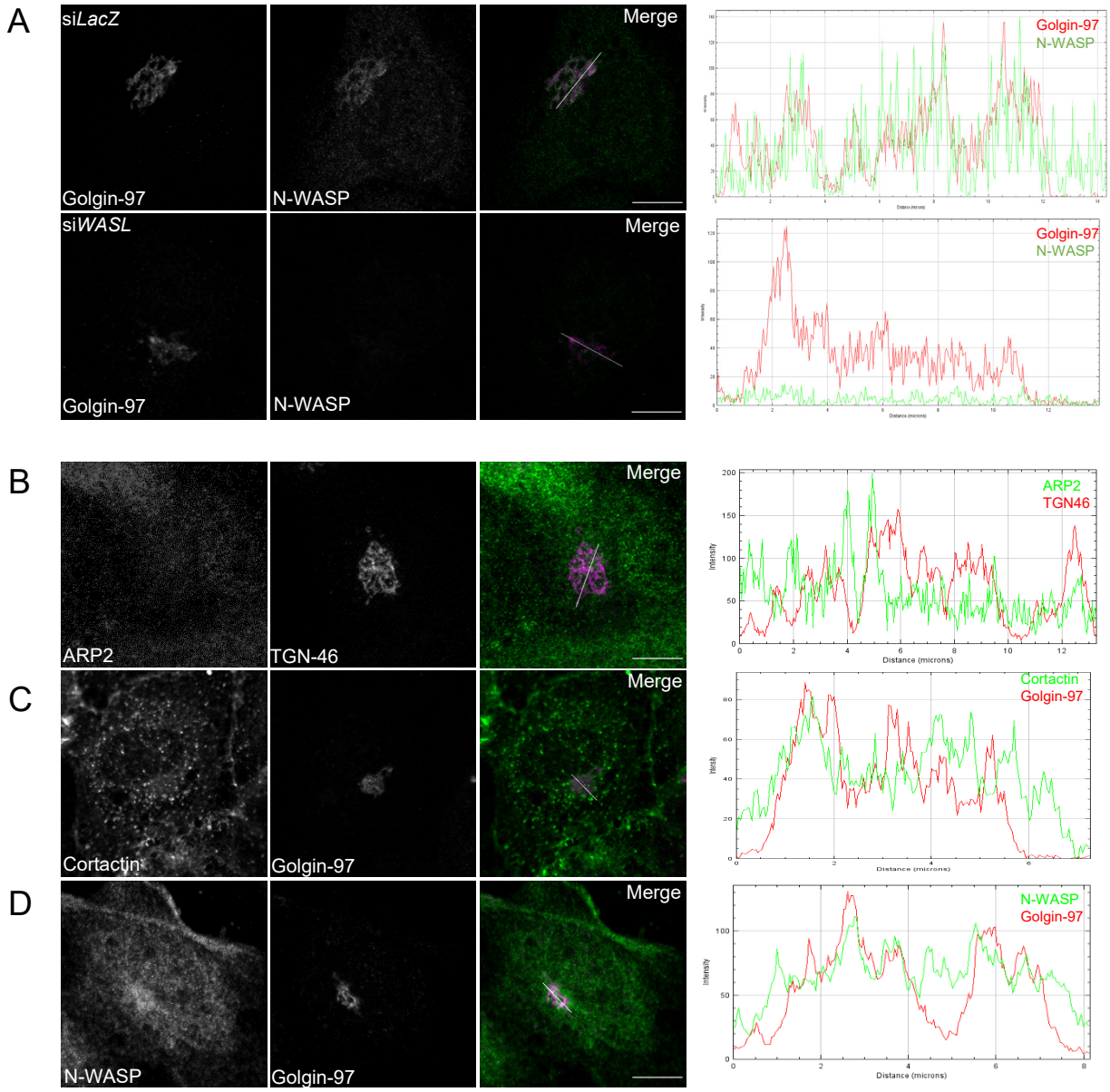

Fig. S1: (A) N-WASP antibody (ab126626) specificity control. HeLa cells were transfected with si*LACZ* or si*WASL*. After 48h cells were stained with anti-N-WASP and Golgin-97 antibodies. Image sections were acquired using a confocal laser scanning microscope. **(B)** ARP2 partially localizes to TGN46-positive structures. Confluent, differentiated HUVEC cell monolayers were stained for endogenous TGN-46 and Arp2. **(C)** Endogenous Cortactin partially localizes to Golgin-97-positive structures in confluent, differentiated HUVEC cell monolayers. **(D)** Endogenous N-WASP partially localizes to Golgin-97-positive structures in confluent differentiated HUVEC cell monolayers. **A-D**, all images depict single confocal sections. Line intensity profiles indicate co-localization. Scale bar*:* 10µm.

Figure S2

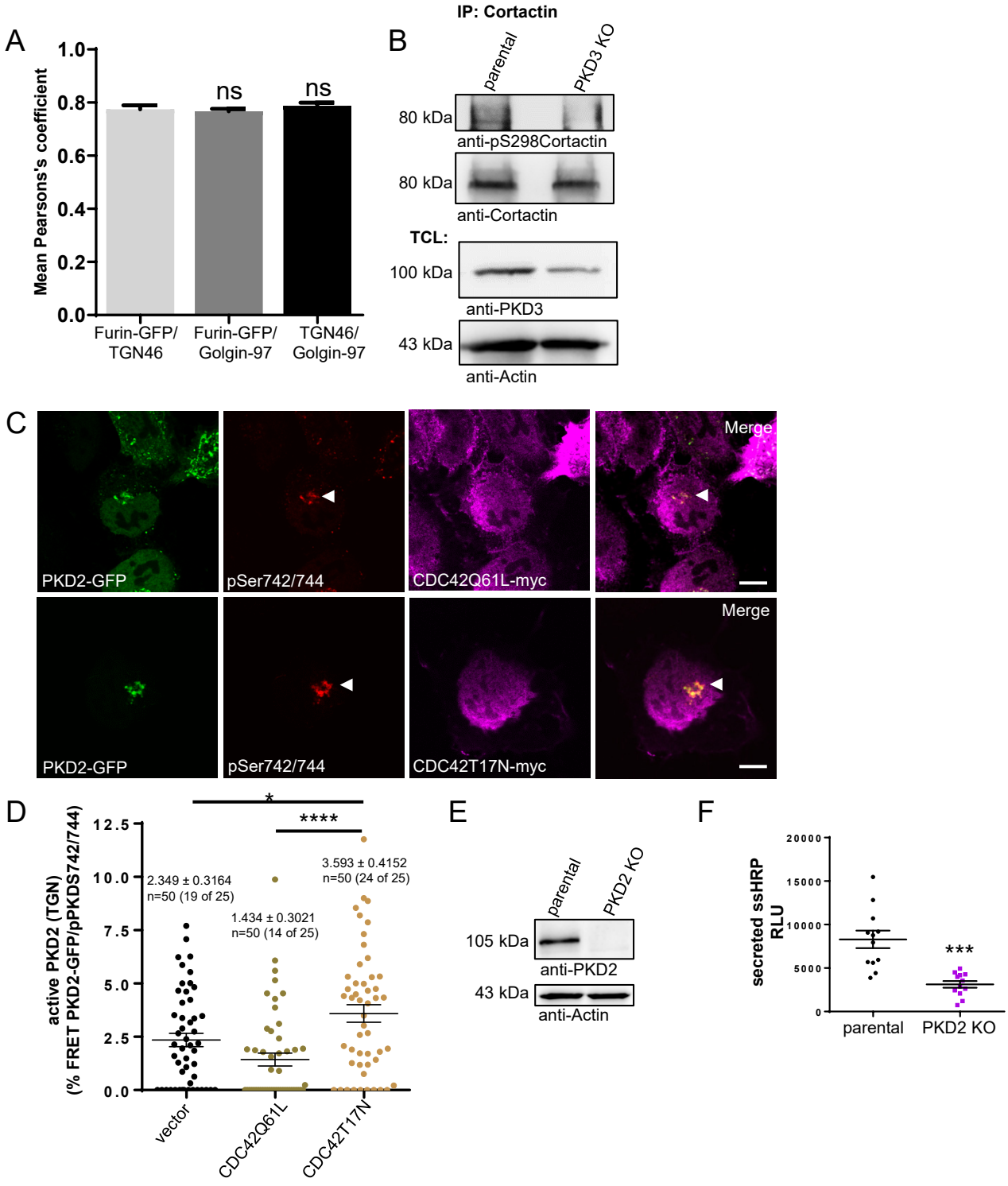

Fig. S2: (A) Quantitative co-localization of Furin-GFP with different TGN markers in HeLa cells. HeLa cells expressing Furin-GFP were stained for endogenous TGN-46 or Golgin-97, or HeLa cells were stained for both, TGN-46 and Golgin-97. The graph shows the mean Pearson's co-localization coefficient ± s.e.m. of three independent experiments from clipped TGN structures using rectangle ROIs around the TGN (n=15 cells). Statistical significance test: ANOVA with Tukey's post-test. ns, not significant. **(B)** PKD3 can phosphorylate endogenous Cortactin in HeLa cells. TCLs of HeLa parental and *PRKD3*-depleted CRISPR cells were subjected to IPs by precipitating endogenous Cortactin. Subsequently, phosphorylation of Cortactin at S298 was probed in Western blots by a specific anti-pS298-Cortactin antibody. IPs were re-probed for Cortactin expression. TCLs were probed for the expression of endogenous PKD3 to demonstrate CRISPR-mediated depletionOne exemplary experiment is depicted. **(C)** Co-expression of inactive CDC42T17N increases perinuclear PKD2 activity. HeLa cells were transfected with PKD2-GFP and vector or CDC42Q61L- and CDC42T17N-myc, respectively. Cells were stained for active PKD using the pPKDS742/744 activation loop antibody, while CDC42 constructs were stained using an anti-myc antibody. Scale bar*:* 10µm. **(D)** Quantitative AB-FRET analysis in cells from **C**. PKD2-GFP activity was probed by detecting FRET with the pPKDS742/744 activation loop antibody labeled with Alexa-568 secondary antibodies, whereas presence of ectopic CDC42 was identified using anti-myc and Alexa-647 antibodies. The graph shows mean ± s.e.m. %FRET of 25 cells and 2 equally sized ROIs used for mean of ROI analysis at PKD2-GFP-positive TGN-structures from three independent experiments (n=50 ROIs). Statistical test: ANOVA with Tukey's post-test. **(E)** Characterization *PRKD2* CRISPR KO cells. TCLs of HeLa parental and *PRKD2* CRISPR KO cells were probed for PKD2 expression. Actin was used as a loading control. **(F)** Knockout of *PRKD2* in HeLa cells reduces secretion of the artificial cargo HRP. Following 16h of ectopic ssHRP expression, HRP was collected in the culture supernatant for 4h and incubated with ECL solution. The graph shows mean ± s.e.m. of 12 independent experiments with four technical replica each. Statistical test: Two-tailed unpaired student's t-test.

Figure S3

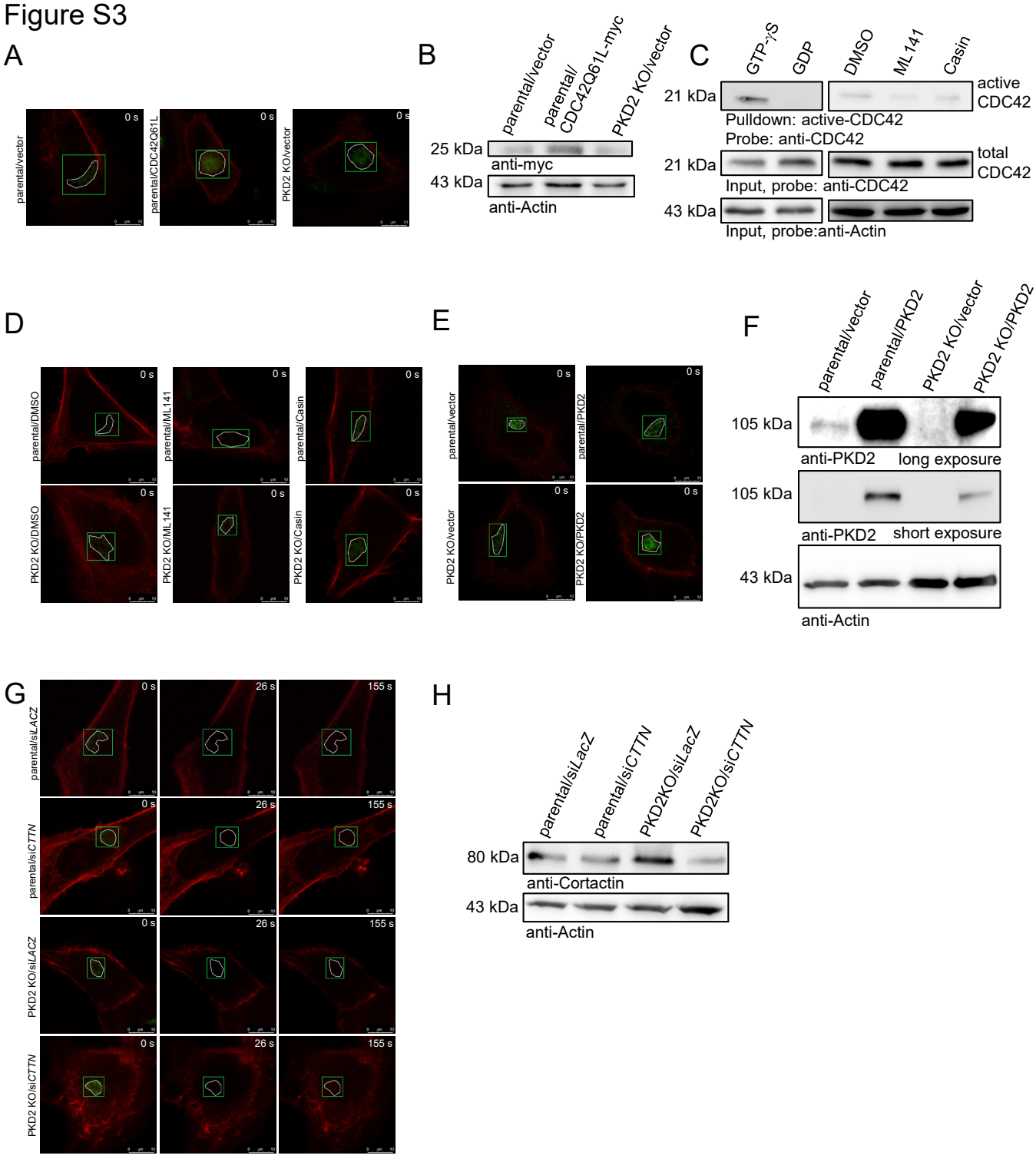

Fig. S3: (A) Exemplary images of cells detected for the indicated conditions in LifeAct-Ruby FRAP experiments in **Fig. 3E, F**. The bleach ROI is depicted in green, whereas the sub-ROI drawn around Furin-GFP-positive structures was used for quantification of steady-state F-actin at the TGN. **(B)** Exemplary expression of CDC42 in TCLs of HeLa cells as used for FRAP experiments in **Fig. 3E, F**. HeLa or HeLa PKD2 KO cells were transfected with Furin-GFP, LifeAct-Ruby and vector or CDC42Q61L-myc. **(C)** CDC42 activity assay. WI-38 cells were treated with DMSO, ML141 (10µM) or Casin (5µM) for 1h. Active CDC42-GTP was pulled down with PBD-beads. GTP-γ-S (1:5) and GDP-loaded CDC42 were used as respective controls. Protein bound to the beads was analyzed by Western Blot. **(D)** Exemplary images of cells detected for the indicated conditions in LifeAct-Ruby FRAP experiments in **Fig. 3G, H**. The bleach ROI is depicted in green, whereas the sub-ROI drawn around Furin-GFP-positive structures was used for quantification of steady-state F-actin at the TGN. **(E)** Exemplary images of cells detected for the indicated conditions in LifeAct-Ruby FRAP experiments in **Fig. 4A, B**. The bleach ROI is depicted in green, whereas the sub-ROI drawn around Furin-GFP-positive structures was used for quantification of steady-state F-actin at the TGN. **(F)** Exemplary expression of PKD2 in TCLs of HeLa cells as used in FRAP experiments in **Fig. 4A, B**. HeLa or HeLa PKD2 KO cells were transfected with Furin-GFP, LifeAct-Ruby and vector or PKD2 overexpression constructs. **(G)** Exemplary images of cells detected for the indicated conditions in LifeAct-Ruby FRAP experiments in **Fig. 4C, D**. T0, first pre-bleach image; T26, first post-bleach image; T155 last image of recovery series. The bleach ROI is depicted in green, whereas the sub-ROI drawn around Furin-GFP-positive structures was used for quantification of steady-state F-actin at the TGN. **(H)** Exemplary expression of Cortactin in TCLs of HeLa cells as used in FRAP experiments in **Fig. 4C, D**. HeLa or HeLa PKD2 KO cells were transfected with si*LACZ* or si*CTTN* and Furin-GFP as well as LifeAct-Ruby. After 48h cells were used for FRAP-experiments or generation of TCLs.

Figure S4

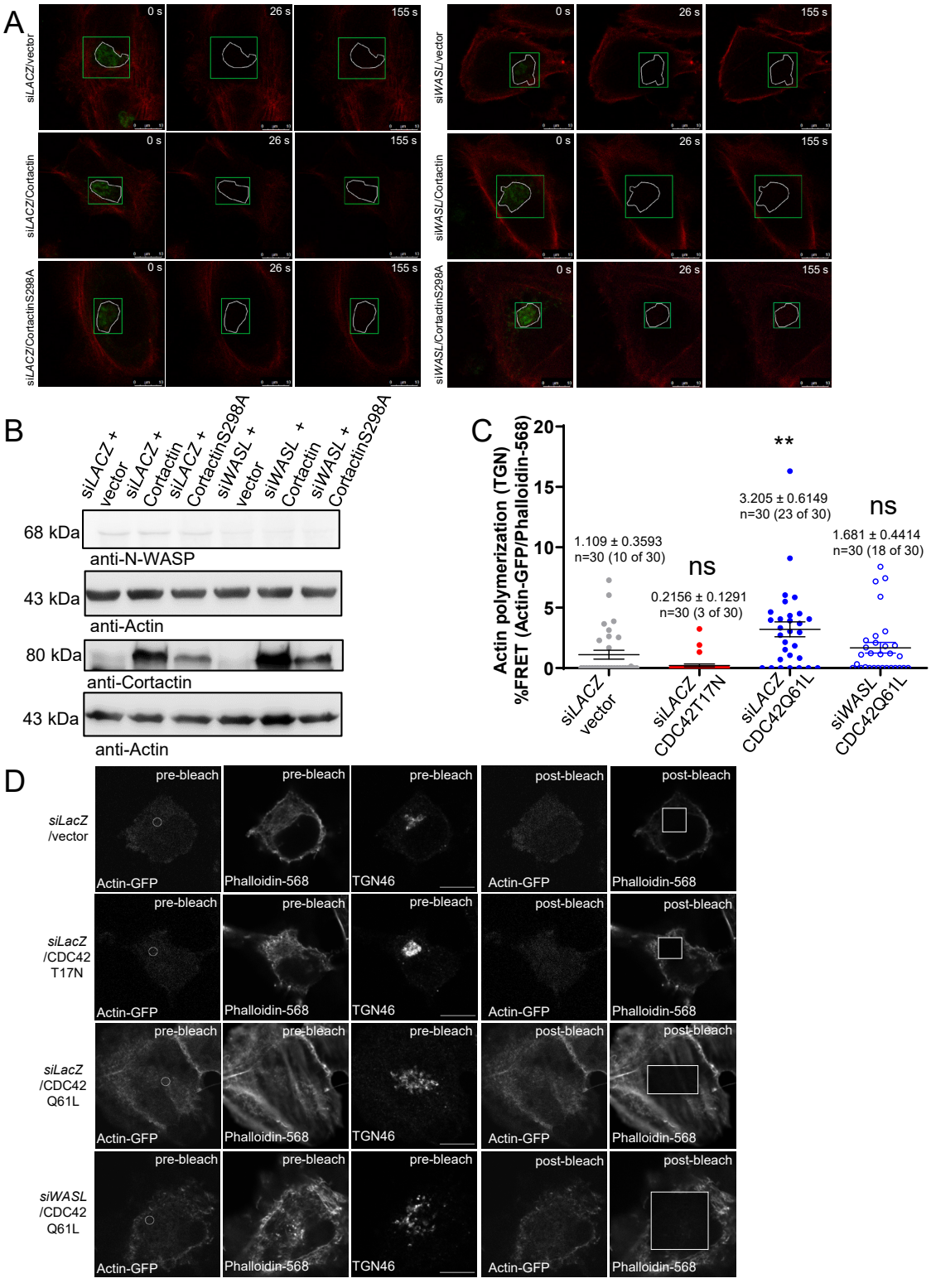

Fig. S4: (A) Exemplary images of cells detected for the indicated conditions in LifeAct-Ruby FRAP experiments in **Fig. 4E, F**. T0, first pre-bleach image; T26, first post-bleach image; T155 last image of recovery series. The bleach ROI is depicted in green, whereas the sub-ROI drawn around Furin-GFP-positive structures was used for quantification of steady-state F-actin at the TGN. **(B)** Exemplary expression of Cortactin and N-WASP in TCLs of HeLa cells as used in FRAP experiments in **Fig. 4E, F**. HeLa cells were transfected with si*LACZ* or si*WASL,* vector, Cortactin-FLAG or CortactinS298A-FLAG, Furin-GFP as well as LifeAct-Ruby. About 30h post transfection cells were analyzed by Western blotting. **(C)** Active CDC42Q61L enhances actin polymerization at the TGN in an N-WASP-dependent manner. Steady-state incorporation of Actin-GFP into Phalloidin-Alexa-568-labeled filaments was quantified by AB-FRET as a measure for relative actin polymerization. HeLa cells were co-transfected with si*LACZ* or si*WASL* and Actin-GFP as well as vector, CDC42T17N or CDC42Q61L, respectively. After 48h cells were processed for IF staining and labeled with Phalloidin-Alexa-568 as well as TGN46-Alexa-647. The graph shows mean ± s.e.m. %FRET of 30 cells with equally sized ROIs used for mean of ROI analysis at TGN-46-positive-Alexa-647-positive structures from three independent experiments (n=30 ROIs). Statistical test: ANOVA with Dunnett's post-test in respect to si*LACZ*/vector. **(D)** Exemplary images of AB-FRET experiments described in **C**. Left-hand side: Pre-bleach images of donor (Actin-GFP), acceptor (Phalloidin-Alexa-568), and the TGN46 as well as the ROI for intensity quantification are shown. Right-hand side: Post-bleach images of donor and acceptor with respective bleach ROIs. Scale bar: 10µm.

Figure S5

A

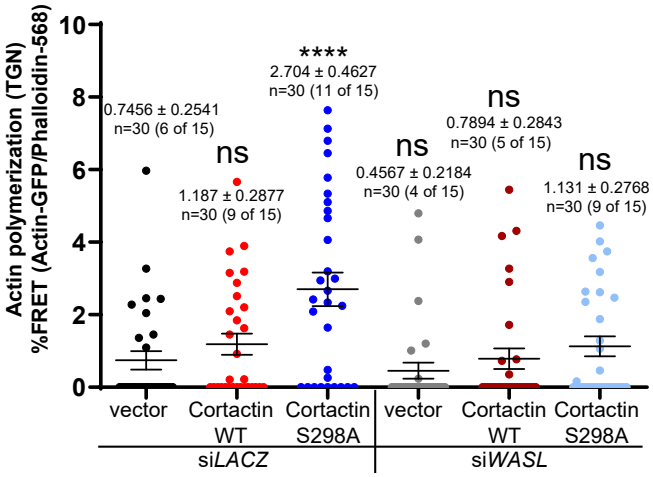

B

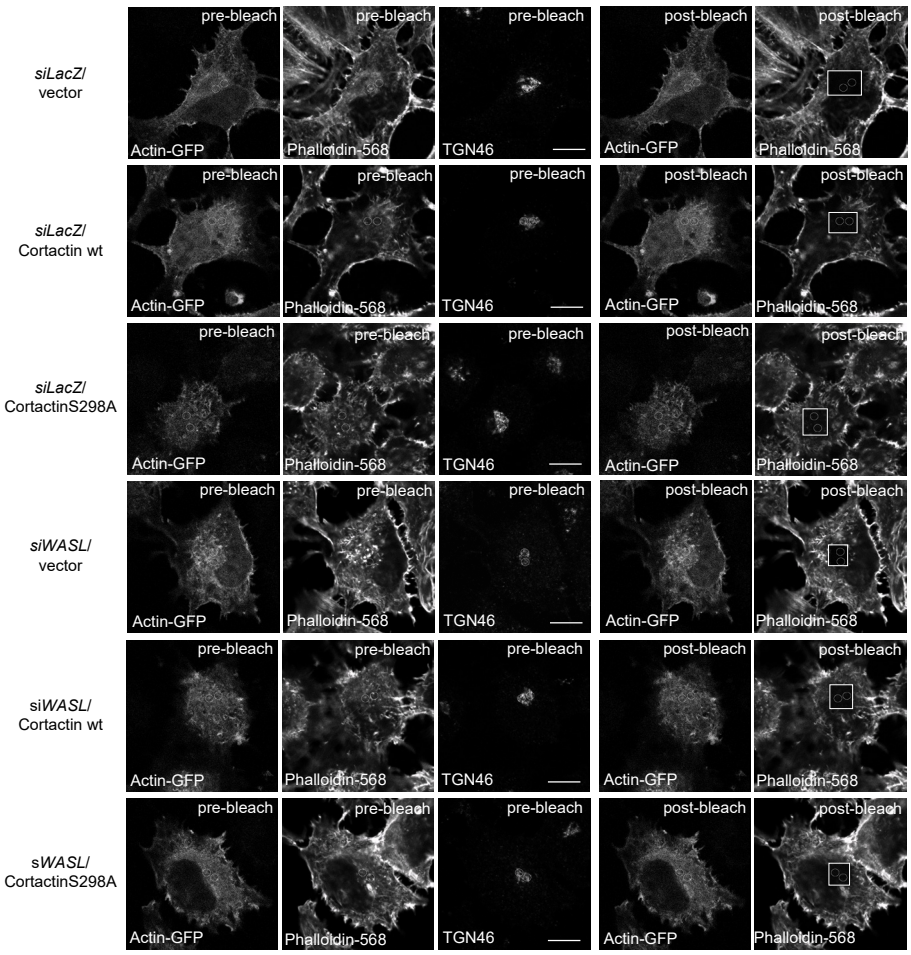

Fig. S5: (A) Non-phosphorylatable-CortactinS298A enhances actin polymerization at the TGN in an N-WASP-dependent manner. HeLa cells were co-transfected with si*LACZ* or si*WASL* and Actin-GFP as well as vector, Cortactin- or CortactinS298A-FLAG, respectively. After 48h cells were processed for IF staining and labeled with Phalloidin-Alexa-568 as well as TGN46-Alexa-647. The graph shows mean ± s.e.m. %FRET of 15 cells and 2 equally sized ROIs used for mean of ROI analysis at TGN46-positive TGN structures from three independent experiments (n=30 ROIs). Statistical significance test: ANOVA with Dunnett's post-test in respect to si*LACZ*/vector. **(B)** Exemplary images of AB-FRET experiments described in **A**. Left-hand side: Pre-bleach images of donor (Actin-GFP), acceptor (Phalloidin-Alexa-568), and the TGN46 (TGN marker) as well as the ROI for intensity quantification are shown. Right-hand side: Post-bleach images of donor and acceptor with respective bleach ROIs. Scale bar: 10µm.

Figure S6

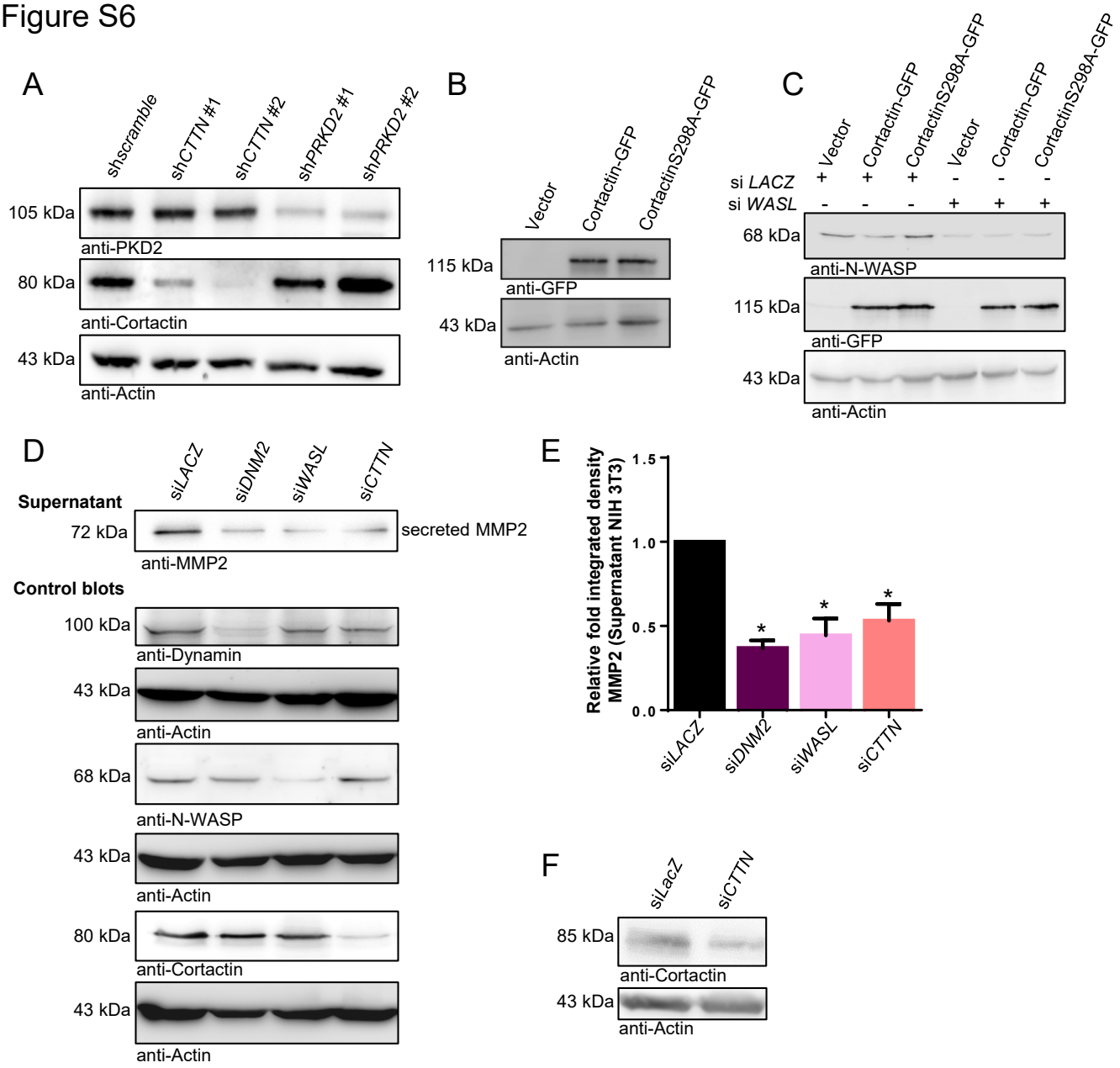

Fig. S6: (A) Knockdown of *CTTN* and *PRKD2* by two different shRNAs in semi-stable HEK293T cell lines used for HRP secretion assays in **Fig. 5A**. **(B)** Example of Cortactin- and CortactinS298A-GFP expression in transiently transfected HEK293T cell lines used for HRP secretion experiments in **Fig. 5B**. **(C)** Verification of the N-WASP knockdown and Cortactin- and CortactinS298A-GFP expression in transiently transfected HEK293T cell lines used for HRP secretion experiments in **Fig. 5E**. **(D)** Depletion of Dynamin2, N-WASP and Cortactin impairs secretion of endogenous MMP2 from NIH 3T3 fibroblasts. NIH 3T3 cells transfected with si*LACZ*, si*DNM2*, si*WASL* and si*CTTN*. After 48h, MMP2 was accumulated in 900µl of serum-free media for 24h. Supernatants analyzed by Western blot for the presence of MMP2 and TCLs for knockdown of Dynamin, N-WASP and Cortactin, respectively. One exemplary experiment of four is shown. **(E)** Statistical analysis of Western blots from **D**. The graph shows mean ± s.e.m. of four independent experiments. Statistical test: ANOVA with Dunnett's post-test towards si*LACZ*. **(F)** Exemplary Western blot show depletion of Cortactin in WI38 pulmonary fibroblasts used in **Fig. 5F, G**.

Figure S7

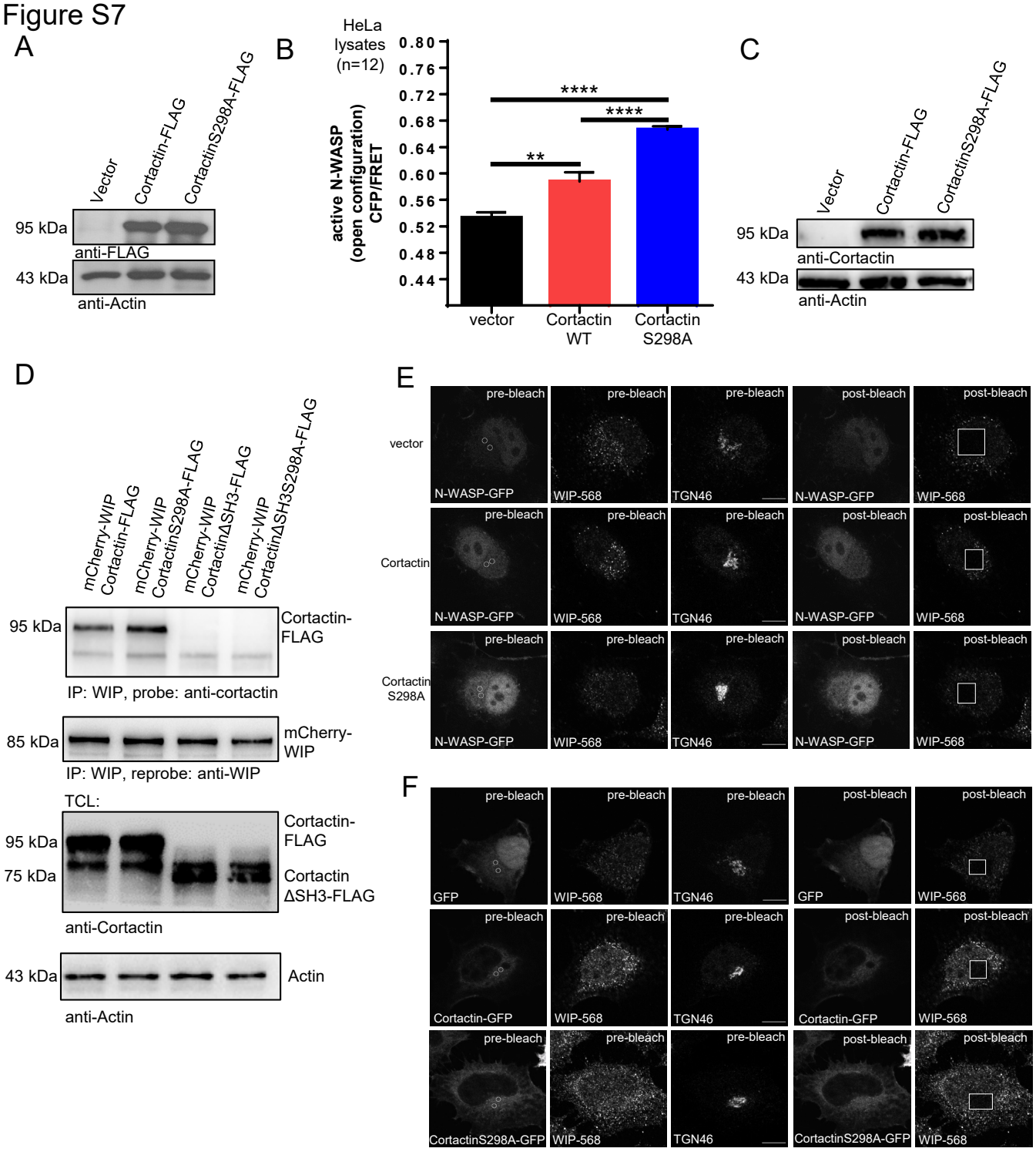

Fig. S7: (A) Expression of Cortactin- and CortactinS298A-FLAG in HEK293T TCLs used for N-WASP-FRET biosensor measurements in **Fig. 6A**. **(B)** Expression of CortactinS298A significantly activates N-WASP in respect to wildtype Cortactin or vector control in HeLa cells. The N-WASP biosensor was co-transfected with the indicated constructs (1:3). After 24h, cells were lysed and fluorescence was measured in cleared lysates using a plate reader. The graph displays relative CFP/FRET ratios for n=12 independently transfected samples. **(C)** Expression of Cortactin- and CortactinS298A-FLAG in HeLa cell lysates used for N-WASP-FRET biosensor measurements in **B**. **(D)** Binding of WIP to Cortactin is enhanced for the non-phosphorylatable-S298A-mutant and dependent on the Cortactin-SH3-domain. HEK293T cells expressing mCherry-WIP and Cortactin-FLAG, CortactinS298A-FLAG, CortactinΔSH3-FLAG or CortactinΔSH3S298A-FLAG were subjected to CoIPs by precipitating WIP, ectopically expressed Cortactin was detected. IPs were re-probed with anti-WIP antibody. The lower panel shows TCLs probed for the expression of the different Cortactin-FLAG constructs. One exemplary experiment is shown. **(E)** Exemplary images of AB-FRET experiments described in **Fig. 7G**. Left-hand side: Pre-bleach images of donor (N-WASP-GFP), acceptor (WIP-Alexa-568), and the TGN46 as well as the ROI for intensity quantification are shown. Right-hand side: Post-bleach images of donor and acceptor with respective bleach ROIs. Scale bar: 10µm. **(F)** Exemplary images of AB-FRET experiments described in **Fig. 7H**. Left-hand side: Pre-bleach images of donor (GFP, Cortactin-GFP, CortactinS298A-GFP), acceptor (WIP-Alexa-568), and the TGN46 as well as the ROI for intensity quantification are shown. Right-hand side: Post-bleach images of donor and acceptor with respective bleach ROIs. Scale bar: 10µm.

Figure S8

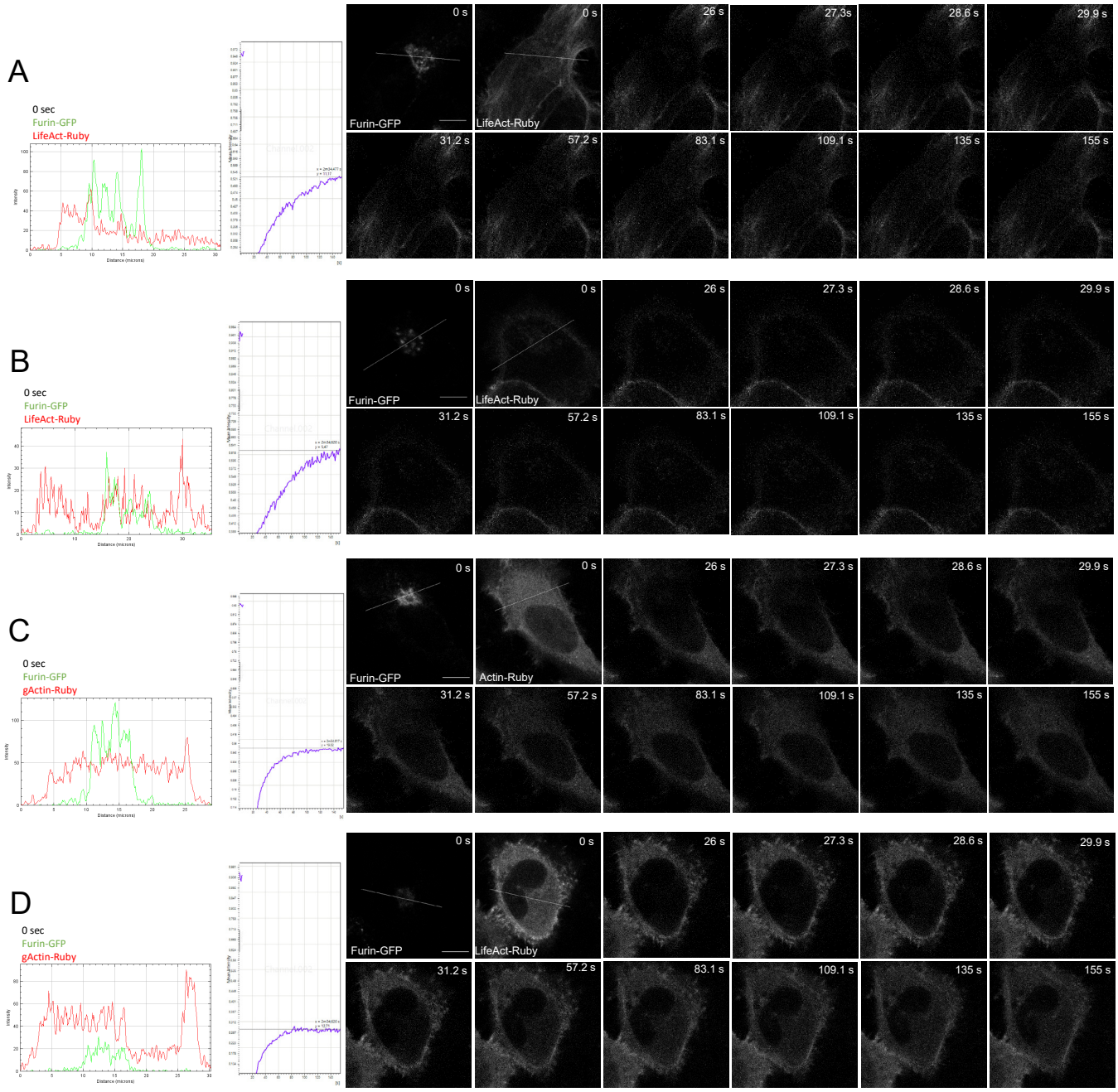

Fig. S8: (A) FRAP curve and respective images of a HeLa cell transfected with plasmids for Furin-GFP, LifeAct-Ruby and vector. **(B)** FRAP curve and respective images of a HeLa cell transfected with plasmids for Furin-GFP, LifeAct-Ruby and CDC42Q61L. **(C)** FRAP curve and respective images of a HeLa cell transfected with plasmids for Furin-GFP, Actin-Ruby and pcDNA vector as control. **(D)** FRAP curve and respective images of a HeLa cell transfected with plasmids for Furin-GFP, Actin-Ruby and CDC42Q61L.

Supplementary movies

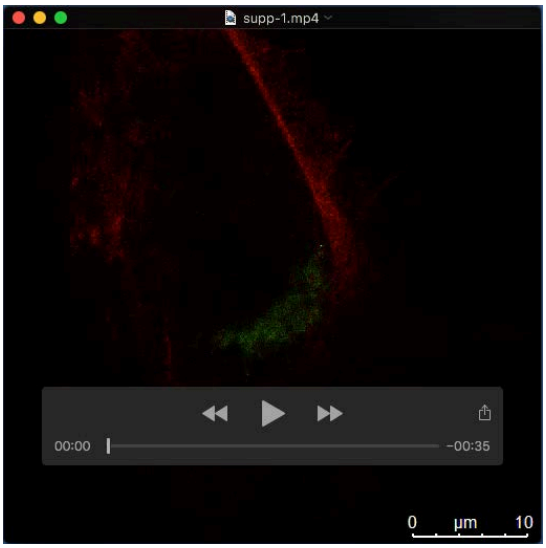

Movie 1. LifeAct-Ruby-FRAP to measure steady-state F-actin formation at the TGN in a HeLa parental/vector control cells. Cells were co-transfected with LifeAct-RubyN143C, Furin-GFP (TGN marker) and the indicated constructs. Images were acquired using a Leica TSC-SP8-HCS confocal laser scanning microscope. Five pre-bleach images; fluorescence recovery: 100 images (130s). Relative-time stamps and scale bar are included in the video sequence.

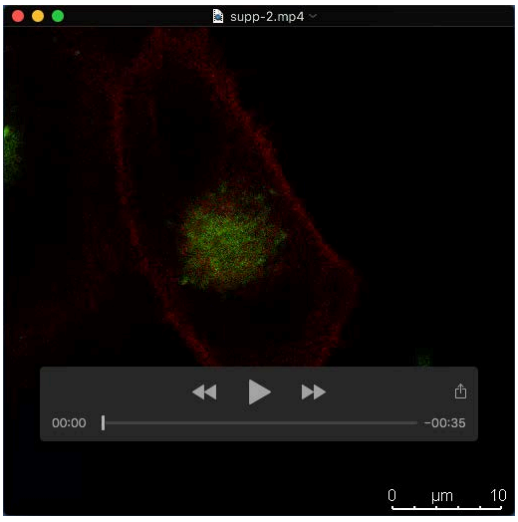

Movie 2. LifeAct-Ruby-FRAP to measure steady-state F-actin formation at the TGN in a HeLa parental/CDC42Q61L cell. Cells were co-transfected with LifeAct-RubyN143C, Furin-GFP (TGN marker) and the indicated constructs. Images were acquired using a Leica TSC-SP8-HCS confocal laser scanning microscope. Five pre-bleach images; fluorescence recovery: 100 images (130s). Relative-time stamps and scale bar are included in the video sequence.

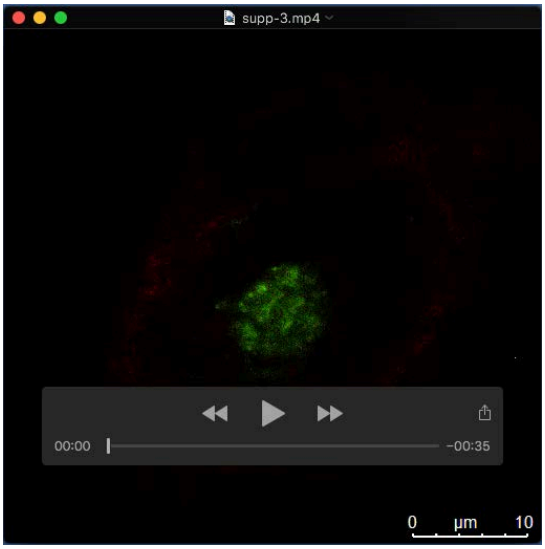

Movie 3. LifeAct-Ruby-FRAP to measure steady-state F-actin formation at the TGN in a HeLa PKD2KO/vector cell. Cells were co-transfected with LifeAct-RubyN143C, Furin-GFP (TGN marker) and the indicated constructs. Images were acquired using a Leica TSC-SP8-HCS confocal laser scanning microscope. Five pre-bleach images; fluorescence recovery: 100 images (130s). Relative-time stamps and scale bar are included in the video sequence.

Movie 4. LifeAct-Ruby-FRAP to measure steady-state F-actin formation at the TGN in a HeLa parental/vector cell. Cells were co-transfected with LifeAct-RubyN143C, Furin-GFP (TGN marker) and the indicated constructs. Images were acquired using a Leica TSC-SP8-HCS confocal laser scanning microscope. Five pre-bleach images; fluorescence recovery: 100 images (130s). Relative-time stamps and scale bar are included in the video sequence.

Journal of Cell Science • Supplementary information

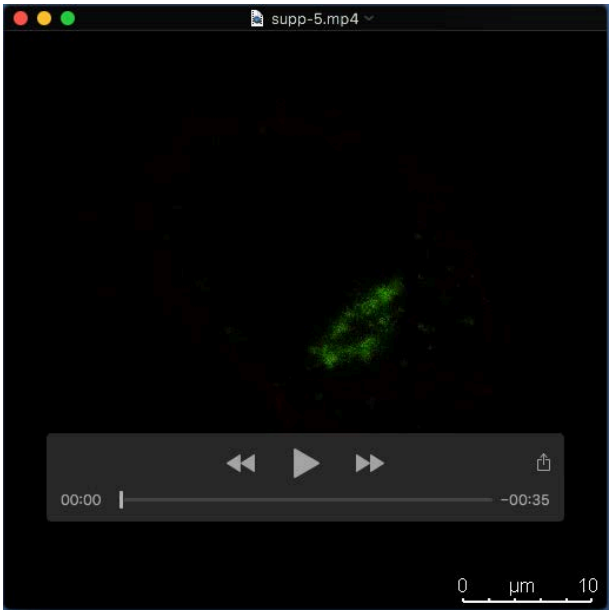

Movie 5. LifeAct-Ruby-FRAP to measure steady-state F-actin formation at the TGN in a HeLa parental/PKD2 cell. Cells were co-transfected with LifeAct-RubyN143C, Furin-GFP (TGN marker) and the indicated constructs. Images were acquired using a Leica TSC-SP8-HCS confocal laser scanning microscope. Five pre-bleach images; fluorescence recovery: 100 images (130s). Relative-time stamps and scale bar are included in the video sequence.

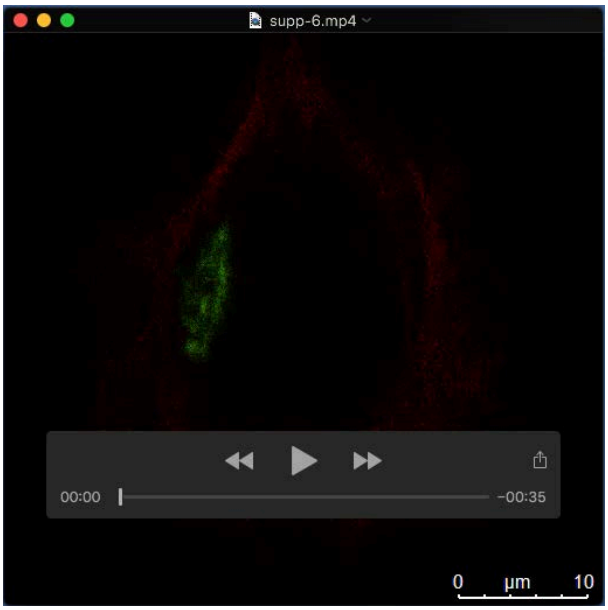

Movie 6. LifeAct-Ruby-FRAP to measure steady-state F-actin formation at the TGN in a HeLa PKD2KO/vector cell. Cells were co-transfected with LifeAct-RubyN143C, Furin-GFP (TGN marker) and the indicated constructs. Images were acquired using a Leica TSC-SP8-HCS confocal laser scanning microscope. Five pre-bleach images; fluorescence recovery: 100 images (130s). Relative-time stamps and scale bar are included in the video sequence.

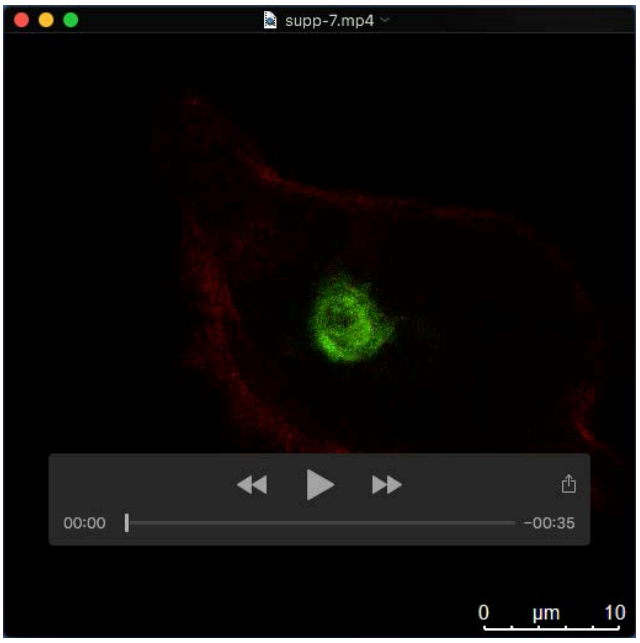

Movie 7. LifeAct-Ruby-FRAP to measure steady-state F-actin formation at the TGN in a HeLa PKD2KO/PKD2 cell. Cells were co-transfected with LifeAct-RubyN143C, Furin-GFP (TGN marker) and the indicated constructs. Images were acquired using a Leica TSC-SP8-HCS confocal laser scanning microscope. Five pre-bleach images; fluorescence recovery: 100 images (130s). Relative-time stamps and scale bar are included in the video sequence.

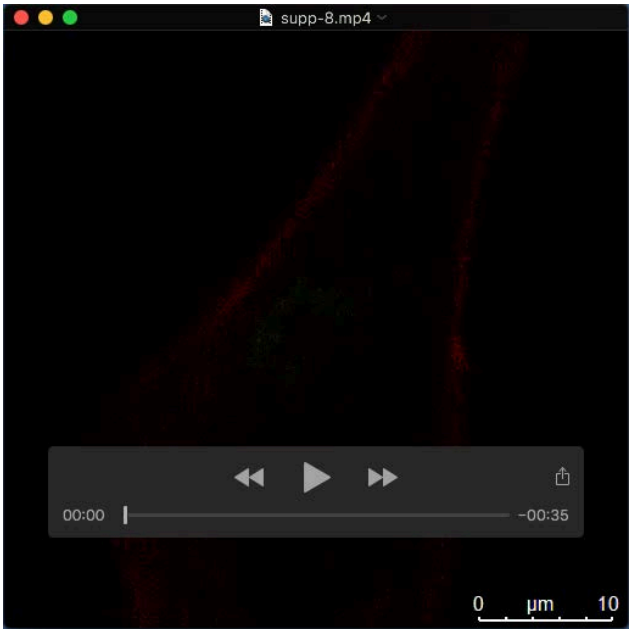

Movie 8. LifeAct-Ruby-FRAP to measure steady-state F-actin formation at the TGN in a HeLa parental/si*LACZ* cell. Cells were co-transfected with LifeAct-RubyN143C, Furin-GFP (TGN marker) and the indicated constructs or siRNAs. After incubation for 48h, images were acquired using a Leica TSC-SP8-HCS confocal laser scanning microscope. Five pre-bleach images; fluorescence recovery: 100 images (130s). Relative-time stamps and scale bar are included in the video sequence.

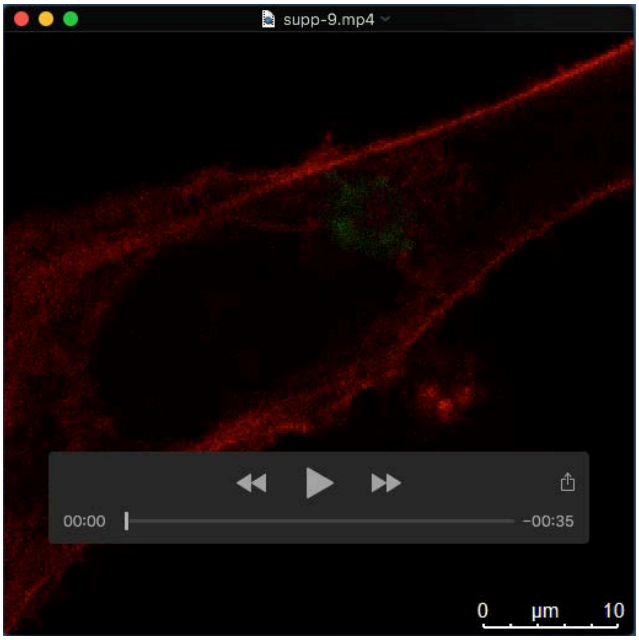

Movie 9. LifeAct-Ruby-FRAP to measure steady-state F-actin formation at the TGN in a HeLa parental/si*CTTN* cell. Cells were co-transfected with LifeAct-RubyN143C, Furin-GFP (TGN marker) and the indicated constructs or siRNAs. After incubation for 48h, images were acquired using a Leica TSC-SP8-HCS confocal laser scanning microscope. Five pre-bleach images; fluorescence recovery: 100 images (130s). Relative-time stamps and scale bar are included in the video sequence.

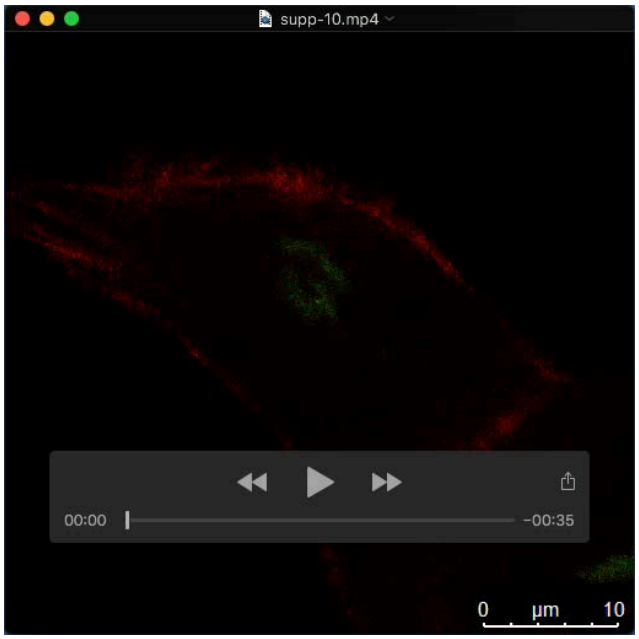

Movie 10. LifeAct-Ruby-FRAP to measure steady-state F-actin formation at the TGN in a HeLa PKD2KO/si*LACZ* cell. Cells were co-transfected with LifeAct-RubyN143C, Furin-GFP (TGN marker) and the indicated constructs or siRNAs. After incubation for 48h, images were acquired using a Leica TSC-SP8-HCS confocal laser scanning microscope. Five pre-bleach images; fluorescence recovery: 100 images (130s). Relative-time stamps and scale bar are included in the video sequence.

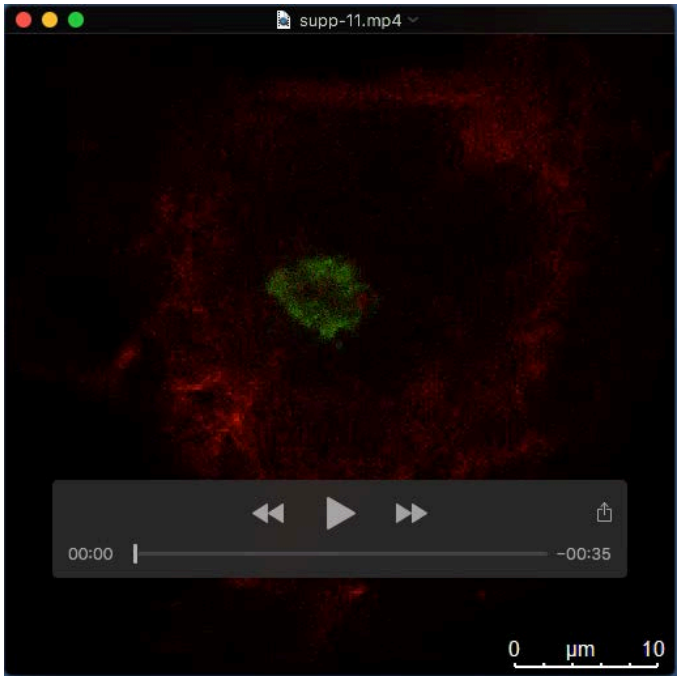

Movie 11. LifeAct-Ruby-FRAP to measure steady-state F-actin formation at the TGN in a HeLa PKD2KO/si*CTTN* cell. Cells were co-transfected with LifeAct-RubyN143C, Furin-GFP (TGN marker) and the indicated constructs or siRNAs. After incubation for 48h, images were acquired using a Leica TSC-SP8-HCS confocal laser scanning microscope. Five pre-bleach images; fluorescence recovery: 100 images (130s). Relative-time stamps and scale bar are included in the video sequence.

Table S1: List of primary and secondary antibodies with ordering numbers, companies and concentrations.

Name	Ordering number	Company	Dilution
Actin	#A5441	Sigma Aldrich, (Taufkirchen, Germany)	WB: 1:2000
Alexa-Fluor 488/568/647 goat-anti-mouse	#A11031 #A11001 #A21235	Thermo Scientific, St. Leon-Rot, Germany	IF: 1:400
Alexa-Fluor 488/568/647 goat-anti-rabbit	# A11034 # A11011 # A21244	Thermo Scientific, St. Leon-Rot, Germany	IF: 1:400
ARP2	#sc-376698	Santa Cruz Biotechnology, Heidelberg, Germany	IF: 1:100 PLA: 1:50
Cortactin (H-191)	#sc-11408	Santa Cruz Biotechnology, Heidelberg, Germany	WB: 1:1000 IF: 1:100 PLA: 1:100
Cortactin (H-5)	#sc-55579	Santa Cruz Biotechnology, Heidelberg, Germany Biotechnology, Heidelberg, Germany	PLA: 1:50
pS298Cortactin	was kindly provided by Johan van Lint, Leuven, Belgium	(De Kimpe et al., 2009)	WB: 1:500
Dynamin	#sc-11362	Santa Cruz Biotechnology, Heidelberg, Germany	WB: 1:1000 IF: 1:100
Flag-M2	#F1804	Sigma Aldrich, Taufkirchen, Germany	WB: 1:2000 IF: 1:100
GFP	#11814460 001	Roche, Basel, Switzerland	WB: 1:2000
Golgin-97	#A21270	Thermo Scientific, St. Leon-Rot, Germany	IF: 1:400

MMP2	#ab37150	Abcam, Cambridge, UK	WB: 1:1000
MMP-2 (D4M2N)	#40994	Cell Signaling Technology, Danvers, USA	IF: 1:100
Myc (9E10)	MABE282	Merck, Darmstadt, Germany	WB: 1:1000 IF: 1:400
N-WASP	#48483	Cell Signaling Technology, Danvers, USA	WB: 1:1000
N-WASP	#ab126626	Abcam, Cambridge, UK	IF: 1:50 PLA: 1:50
PKD2	ST1042	Merck, Darmstadt, Germany	WB: 1:1000
pPKDS742/744	#2054	Cell Signaling Technology, Danvers, USA	IF: 1:100
pPKDS916	#2051	Cell Signaling Technology, Danvers, USA	WB: 1:2000 IF: 1:100
TGN-46	#AP326910SU-N	Acris (OriGene Technologies, Rockville, MD, USA)	IF: 1:400
WIP (A-7)	#sc-271113	Santa Cruz Biotechnology, Heidelberg, Germany	IF: 1:100 WB: 1:1000
WIP (C-1)	#sc-390099	Santa Cruz Biotechnology, Heidelberg, Germany	WB: 1:1000 IP: 2.5µg/sample

References

De Kimpe, L., Janssens, K., Derua, R., Armacki, M., Goicoechea, S., Otey, C., Waelkens, E., Vandoninck, S., Vandenheede, J. R., Seufferlein, T. et al. (2009). Characterization of cortactin as an in vivo protein kinase D substrate: interdependence of sites and potentiation by Src. *Cell Signal* **21**, 253-63.

Table S2: List of cDNA expression vectors, shRNAs, siRNAs and sequencing primers

Name	Source	Reference
cDNA expression vectors		
pCR3.V62-Met-Flag-Cortactin	A. Hausser, University of Stuttgart, Germany	(Eiseler et al., 2010)
pCR3.V62-Met-Flag-CortactinS298A	A. Hausser, University of Stuttgart, Germany	(Eiseler et al., 2010)
pcDNA3-FLAG-CortactinΔSH3	this study	
pcDNA3-FLAG-CortactinΔSH3-S298A	this study	
pEGFP-N1-Cortactin	A. Hausser, University of Stuttgart, Germany	(Eiseler et al., 2010)
pEGFP-N1-CortactinS298A	A. Hausser, University of Stuttgart, Germany	(Eiseler et al., 2010)
N-WASP-GFP	Ralf Kemkemer, Max Planck Institute for Medical Research	-
pEGFP-N1-PKD2	A. Hausser, University of Stuttgart, Germany	(Hausser et al., 2002; Hausser et al., 2005; Wille et al., 2014)
pmRuby-Actin7	F. Oswald, Ulm University, Germany	
pcDNA3-LifeAct-mRubyN143C	F. Oswald, Ulm University, Germany	
Furin-GFP	T. Seufferlein, Ulm University, Germany	
pRK5-myc-Cdc42Q61L	Addgene No: 12974	
pRK5-myc-Cdc42T17N	Addgene No: 12973	
pcDNA3-PKD2	A. Hausser, University of Stuttgart, Germany	(Hausser et al., 2002; Hausser et al., 2005; Wille et al., 2014)
CFP-N-WASP-YFP FRET activity sensor	John Condeelis, Albert-Einstein College of Medicine, NY, USA	(Lorenz et al., 2004)
pmCherry-C1 hWIP	Addgene No: 29573	(Cortesio et al., 2010)
siRNAs		

si*LacZ* 5‘-GCGGCUGCCGGAAUUUACC-3‘	Eurofins Genomics, Ebersberg, Germany	(Eiseler et al., 2010; Wille et al., 2014; Ziegler et al., 2011)
si*WASL* (Hs_*WASL*_6) cat.: SI02664263 5’-GAUACGACAGGGUAUCCAAtt-3’	Quiagen, Hilden, Germany	
si*PRKD*2 (s24646), cat.: 4390824 5‘-AGAUGAUCCUGUCCAGUGAtt-3‘	Thermo Scientific, St. Leon-Rot, Germany	
si*CTTN,* human (s4667), cat.: 4392420 5‘-CCAACAUCGAGAUGAUUGAtt-3‘	Thermo Scientific, St. Leon-Rot, Germany	
si*DMN2* (s65068), cat.: 4390815 5’-GGACCUUCGACAGAUUGAAtt-3’	Thermo Scientific, St. Leon-Rot, Germany	
si*CTTN*, mouse (s64627), cat.: 4390771 5’-GAAUCCCAAAAAGACUAUAtt-3’	Thermo Scientific, St. Leon-Rot, Germany	
si*WASL*, mouse (s91559), cat.: 4390771 5’-GGGAUGCGCUUUUAGACCAtt-3’	Thermo Scientific, St. Leon-Rot, Germany	
shRNA		
pLKO.1-puro sh *scramble* (Mission shRNA, Sigma shc002)	Sigma Aldrich, Taufkirchen, Germany	
shCTTN #1: pLKO.1-puro sh *CTTN* (NM_005231, TRCN0000040274)	Thermo Scientific, St. Leon-Rot, Germany	
sh*CTTN* #2: pLKO.1-puro sh *CTTN* (NM_005231, TRCN0000040273)	Thermo Scientific, St. Leon-Rot, Germany	
shPRKD2 #1 pLKO.1-puro sh *PRKD2* (NM_016457.x-1720s1c1)	Sigma Aldrich, Taufkirchen, Germany	
sh*PRKD2* #2 pLKO.1-puro sh *PRKD2* (NM_016457.x-294s1c1)	Sigma Aldrich, Taufkirchen, Germany	
Genomic sequencing primer		
PRKD2 sequencing forward primer: 5‘ GAAGGCGGCTCTGAGCTTTTC 3‘	biomers.net, Ulm, Germany	
PRKD2 sequencing reverse primer: 5’ GCCACCACCTCTCACCCGACAG 3’	biomers.net, Ulm, Germany	

References

Cortesio, C. L., Perrin, B. J., Bennin, D. A. and Huttenlocher, A. (2010). Actin-binding protein-1 interacts with WASp-interacting protein to regulate growth factor-induced dorsal ruffle formation. *Mol Biol Cell* **21**, 186-97.

Eiseler, T., Hausser, A., De Kimpe, L., Van Lint, J. and Pfizenmaier, K. (2010). Protein kinase D controls actin polymerization and cell motility through phosphorylation of cortactin. *J Biol Chem* **285**, 18672-83.

Hausser, A., Link, G., Bamberg, L., Burzlaff, A., Lutz, S., Pfizenmaier, K. and Johannes, F. J. (2002). Structural requirements for localization and activation of protein kinase C mu (PKC mu) at the Golgi compartment. *J Cell Biol* **156**, 65-74.

Hausser, A., Storz, P., Martens, S., Link, G., Toker, A. and Pfizenmaier, K. (2005). Protein kinase D regulates vesicular transport by phosphorylating and activating phosphatidylinositol-4 kinase IIIbeta at the Golgi complex. *Nat Cell Biol* **7**, 880-6.

Lorenz, M., Yamaguchi, H., Wang, Y., Singer, R. H. and Condeelis, J. (2004). Imaging sites of N-wasp activity in lamellipodia and invadopodia of carcinoma cells. *Curr Biol* **14**, 697-703.

Wille, C., Kohler, C., Armacki, M., Jamali, A., Gossele, U., Pfizenmaier, K., Seufferlein, T. and Eiseler, T. (2014). Protein kinase D2 induces invasion of pancreatic cancer cells by regulating matrix metalloproteinases. *Mol Biol Cell* **25**, 324-36.

Ziegler, S., Eiseler, T., Scholz, R. P., Beck, A., Link, G. and Hausser, A. (2011). A novel protein kinase D phosphorylation site in the tumor suppressor Rab interactor 1 is critical for coordination of cell migration. *Mol Biol Cell* **22**, 570-80.

Table S3: Raw data for AB-FRET experiments

Click here to Download Table S3